29 MeV π ELASTIC SCATTERING DIFFERENTIAL CROSS SECTION RATIO OF $^{12}C/^{13}C$.

by

WILLIAM GYLES
B.Sc. University of Manchester, 1976

A THESIS SUBMITTED IN PARTIAL FULFILLMENT OF THE
REQUIREMENTS FOR THE DEGREE OF
MASTER OF SCIENCE

in

THE FACULTY OF GRADUATE STUDIES
Department of Physics

We accept this thesis as conforming
to the required standard

THE UNIVERSITY OF BRITISH COLUMBIA
August, 1979

In presenting this thesis in partial fulfilment of the requirements for an advanced degree at the University of British Columbia, I agree that the Library shall make it freely available for reference and study. I further agree that permission for extensive copying of this thesis for scholarly purposes may be granted by the Head of my Department or by his representatives. It is understood that copying or publication of this thesis for financial gain shall not be allowed without my written permission.

Department of PHYSICS

The University of British Columbia
2075 Wesbrook Place
Vancouver, Canada
V6T 1W5

Date 23-10-79

ABSTRACT

The large fluxes of positive and negative pions available in meson factories over the last few years have lead to an accumulation of precise π-nuclear data over wide ranges in energy and atomic number. Little nuclear structure information has been extracted from the data since a microscopic model for the pion interaction in the nucleus is not fully developed. However the elastic scattering differential cross sections for low energy pions are predicted well over a wide range of atomic mass using a potential in which some parameters are empirically derived. Since the potential is semi-empirical some nuclear structure information can not reliably be derived directly from the data. Measurement of differences in the nuclear structure between neighbouring nuclides, however, should be reliable if the potential produces the correct variation of differential cross section in this mass region.

In the experiment reported here the differential cross section ratio for elastic scattering of 29 MeV π^- on $^{13}C/^{12}C$ is measured using scintillator range telescopes. Solid carbon targets of pressed powder were used. Since only a relative measurement is made the errors in the ratio are statistical only.

A large peak in the distribution of the cross section

ratio is produced by changes in the s-p interference minimum between ^{12}C and ^{13}C. The cross section ratio is sensitive to the neutron distribution of ^{13}C because of the large s-wave interaction of the pion with neutrons in the nucleus. A measurement of the neutron rms. radius of ^{13}C and some tests of dependence on the shape of the neutron distribution and optical potential parameters are made. The neutron distribution rms. radius of ^{13}C is found to be 2.365±.025 fm.

Table of Contents

List of Tables

List of Figures

ACKNOWLEDGEMENTS

I am pleased to have this opportunity of thanking my Research Supervisor, Dr. Richard R. Johnson, for his guidance and encouragement during the course of this work.

I would also like to express my thanks to the other members of the PISCAT group, for their valuable assistance, and to the Batho Memorial Biomedical Facility, for the use of their pion channel.

CHAPTER I

Introduction

Since the advent of the meson factories (LAMPF, TRIUMF, SIN) a great deal of data on low energy pion-nucleus scattering has accumulated . Pion-nucleus optical potentials have been developed to the extent that they can reasonably predict the cross sections for elastic scattering over a wide energy range and over a large spread in atomic weight . Part of the impetus for this effort has been the possibility of studying nuclear structure with pions, but so far this goal has hardly been achieved. The pion-nucleus interaction has proved to be a complex mechanism requiring many factors to be taken into account to produce fits to the data. This, coupled with the lack of structure in the cross sections, makes it difficult to separate nuclear structure effects from the uncertainties in the interaction. In particular, if optical potential parameters are fitted to experimental pion-nucleus data, the nuclear structure information that can then be extracted from the fit is limited.

Ideally, a potential would be derived strictly from consideration of the multiple scattering of a pion in the nucleus and all parameters for such a potential derived from the pion-nucleon scattering amplitudes . It is necessary, however , to include such nuclear effects as absorption on two nucleons[1] and short range correlations between nucleons[1,2] (the Ericson-Ericson/Lorentz-Lorenz effect). This introduces parameters that are usually determined by pion-nucleus

experiments[3,4,5,6,7]. Since the cross sections generally show little structure, variations in the parameters may mimic nuclear structure details such as density distributions , so these details can not reliably be derived directly from the experimental cross section.

The experiment reported here measures differential cross section ratios of π^- on ^{12}C and ^{13}C at 29 MeV. By making a relative measurement it is suggested that nuclear structure effects can be isolated. Inaccuracies in the potential used should cancel to a large extent. Any systematic measurement errors will also cancel each other out, thus removing normalisation errors and virtually eliminating the problem of long term instabilities in the apparatus. Systematic measurement errors in the ratio are thus negligible compared to statistical errors. In Chapter IV ,a comparison of the differential cross sections of ^{12}C and ^{13}C shows the neutron distribution of ^{13}C.

Discrepancies exist at present between neutron rms. radii measured using different techniques. For example, in Table I is a summary of recent experimental values of $\Delta r = r_n - r_p$ in ^{48}Ca (table taken from reference 8). Hartree-foch calculations[16] predict $\Delta r \sim 0.2$ fm. , which agrees only with the high energy proton and α particle results. Accurate and reliable values of r_n would be a useful test for theoretical approximations used in density dependent Hartree Foch calculations.

The pion might seem to be an obvious choice for studying neutron distributions because of its different interactions with neutrons and protons. Indeed several attempts have been

Table I. Results for $\Delta r = r_n - r_p$ of ^{48}Ca.
Taken from Varma and Zamick.[8]

Method		Δr (fm)	Ref.
p scattering	1.05 GeV	.19±.05	9
	1.0 GeV	.21±.05	10
	10.8 to 16.3 MeV	.39±.10	11
α elastic scattering	79 MeV	.03±.08	12
	166 MeV	.38±.12	13
	1.37 GeV	.20±.06	14
π total cross sections	90 to 240 MeV	.08±.05	15

made to exploit the isovector nature of the pion-nucleon interaction in this way. Ratios of π^+ and π^- total cross sections were measured[17,18] at energies near 1 GeV. At this energy, the π^-p (or π^+n) interaction is about 3 times stronger than the π^-n (or π^+p) interaction. The ratio σ^+/σ^-, however, is insensitive to reasonable variatons in the neutron density distributions. Because of this insensitivity and because of the dependence on calculations of Coulomb effects, the density distributions extracted from these measurements are not reliable.

When measuring the differences in radii between neighbouring isotopes many uncertainties in the experiment and theory are cancelled. This method was used by Cooper[19] to extract neutron rms radii for ^{18}O and ^{48}Ca by comparing their pion total cross sections in the 100-200 MeV range with those of ^{16}O and ^{40}Ca respectively. At these energies, the nucleus is essentially a black disc because of the strong 3,3 resonance, thus the results were considered insensitive to the interaction model used. Jansen et al[20] have compared π^+ and π^- elastic scattering differential cross sections from ^{18}O and ^{48}Ca at the 3,3 resonance and extracted neutron radii. As the interaction is so strong the pion samples only the surface of the nucleus, so the cross sections are not sensitive to low moments of the distribution such as the rms. radius. A matter distribution model must be used to relate the effective radius to the rms. value. As pointed out by Sternheim and Yoo[21], however, the neutron rms. radii extracted depend upon the particular set of optical parameters used. This is caused by the simple

diffractive nature of the scattering, which is determined largely by the product of k, the wavenumber in the nucleus, and r, the effective radius at which the absorption occurs. Changes in the absorptivity cause changes in the effective radius of the nucleus, thus leading to fits for different neutron rms. radii. Changes in the real part of the potential also affect the value of k, again giving fits for different radii. A necessary requirement is that the potential should also predict the measured total cross section if it is to independantly fix the potential parameters.

One can alleviate this problem by using pions of lower energy away from the 3,3 resonance. Here the nucleus is not so absorptive, and the cross section data are not generally diffractive. Dytman et al.[22] measured the differential cross section ratio cf ^{12}C and ^{13}C with 50 MeV π^+. Fig. 1 shows that the distribution is quite flat with only a small peak at low angles caused by a shift in the s,p interference minimum. It may be anticipated, by considering the free π-nucleon scattering amplitude, that a larger effect would be produced with π^-. The scattering amplitude may be parametrised

$$f(\theta) = b_0 + b_1 \tilde{t}.\tilde{\tau} + (c_0 + c_1 \tilde{t}.\tilde{\tau})\ \tilde{k}.\tilde{k}' \quad ,$$

neglecting a small spin dependent term, and where the coefficients

b_0 = s-wave isoscaler scattering length = -.005 fm

b_1 = s-wave isovector scattering length = -.13 fm

c_0 = p-wave isoscaler scattering volume = .64 fm^3

c_1 = p-wave isovector scattering volume = .43 fm^3

are determined from the π-N scattering lengths[23].

Figure 1. Elastic Scattering Differential Cross Section Ratios of 50MeV π^+ on $^{13}C/^{12}C$. Data from Dytman.[22]

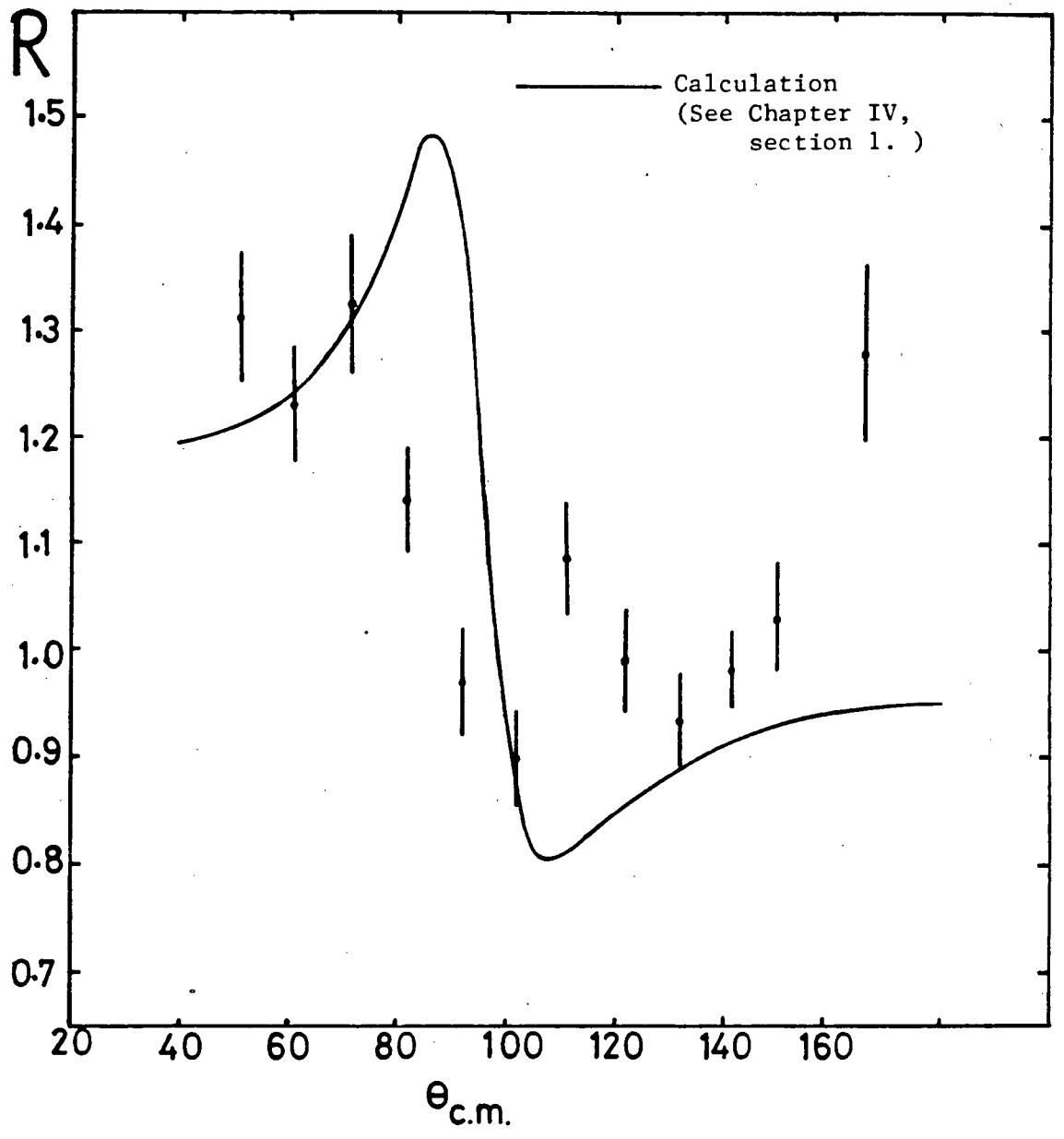

$\tilde{k}$ and $\tilde{k}'$ are the wavevectors of the incoming and outgoing pion. $\tilde{t}$ and $\tilde{\tau}$ are the isospin vectors of the nucleon and pion. $\tilde{t}.\tilde{\tau}$ =+1 for π^+p or π^-n and -1 for π^-p or π^+n.

For the isoscaler nucleus, ^{12}C, only the isoscaler terms contribute . For π^+n, the isoscaler and isovector amplitudes cancel to a large extent, and the extra neutron of ^{13}C will not have a large effect on the π^+ cross section. With π^-, however, the isoscaler and isovector amplitudes add. The relative proportions of s and p wave are altered from the completely isoscaler case because of the large s-wave isovector amplitude, therefore a large change in the s-p interference minimum may be expected. Since the isovector amplitudes are effective only where there is a neutron or proton excess , the π^- should be sensitive to the difference between proton and neutron radii.

CHAPTER II

Apparatus and Experimental Technique.

1. a) Apparatus

The experiment was performed on the TRIUMF biomedical pion beamline , M8. A sketch of the beamline is shown in Fig. 2. The pion kinetic energy of the beam was 30 MeV with $\Delta p/p=4.2\%$. Particle fractions were pions=13%, muons=3% and electrons=84%. The proton current during the week's run was typically 7μA, giving a pion flux of about 1.4×10^5 s^{-1} .

The beam flux was monitored primarily with a gas ionization chamber, open to the atmosphere, placed directly after the last quadrupole. Although the ionization chamber was calibrated to 1% accuracy[24], the calibration was not needed for the ratio measurement, the only requirement being that it should be stable over the time required to perform the measurements on the three targets (about 3 to 5 hours) . The beam was also monitored after the target by a pair of large plastic scintillators, M1 and M2, used in coincidence to eliminate protons, arising from the target, which stop in the first counter. The scintillators also determined the muon and electron contaminations by measuring the flight time of the particles from a capacitive pickup placed in front of the pion production target, T2, in the primary proton beam. A time-of-flight spectrum taken this way shows π^-'s, μ's and e's clearly separated in time (Fig. 3).

A pair of wire chambers giving X and Y beam profiles were mounted behind the scintillators M1 and M2. They were triggered

Figure 2. M8 Beamline.

Channel length	8 m take-off angle 30°
Momentum range	0 - 220 MeV/c
Momentum acceptance	±6.7% ΔP/P FWHM
Momentum resolution	1.5% ΔP/P FWHM
Polarity	π^+ or π^-
π flux at 180 MeV/c, full momentum acceptance 10 cm Be target	8×10^6 π^+/sec/μA proton 1.3×10^6 π^-/sec/μA proton
Contamination at 180 MeV/c π^- 10 cm cooled Be target	~24% electrons ~11% muons
Dose rate to a 5 × 5 × 5 cc field	~0.2 rad/min/μA proton

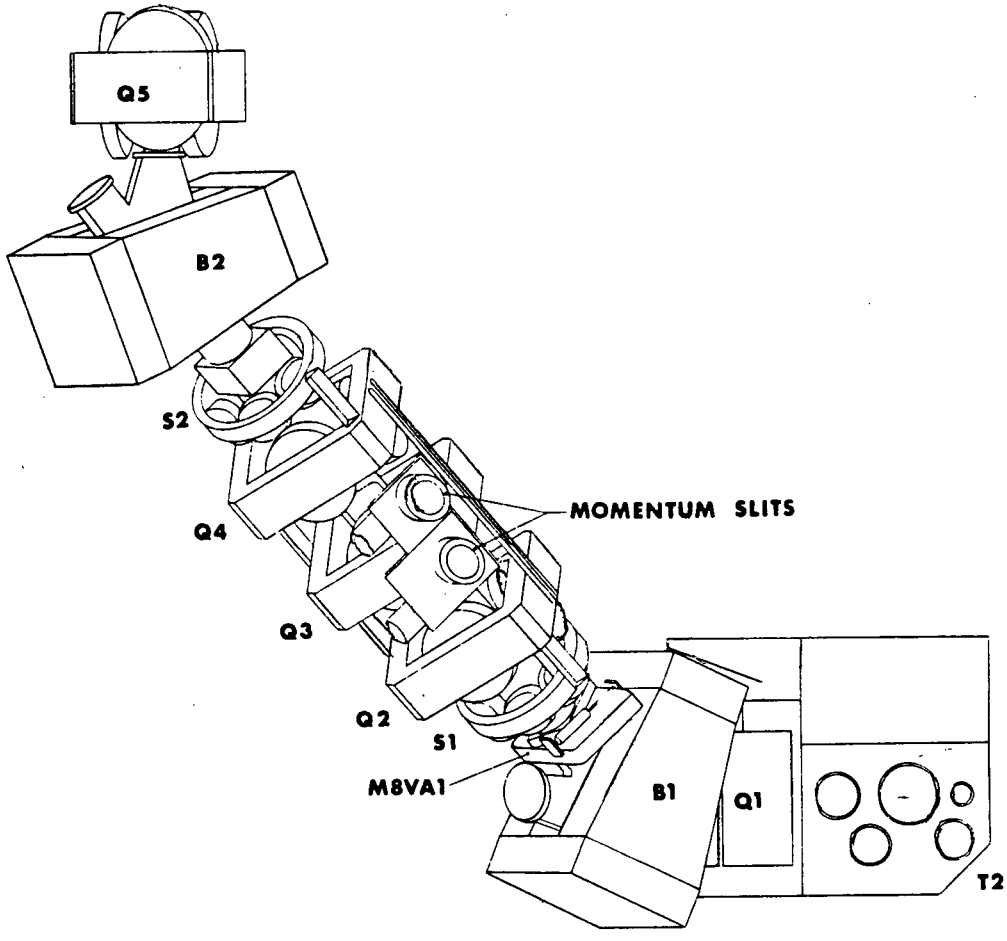

Figure 3. Time of Flight Spectrum of Incident Beam.

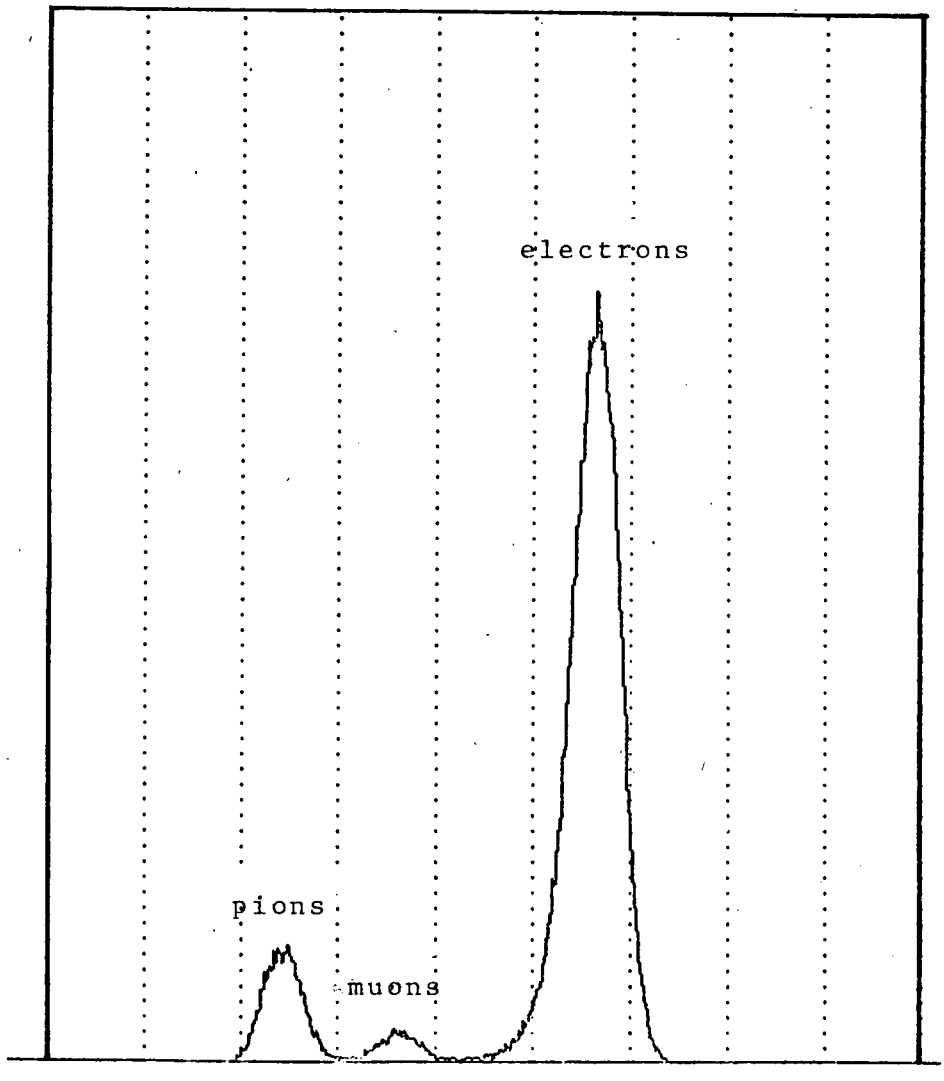

by the coincidence M1•M2 . The wire chambers and scintillators, mounted on rails, could be slid along the beam direction. Beam profiles were taken, with the corresponding beam tune, for both target positions. The beam profiles at the target positions are shown in Fig. 4 along with a contour plot generated by an on-line program. Profiles were also taken at intervals along the beam to estimate the beam divergence , which was found to be approximately ±1.4°.

Fig. 5 is a diagram of the experimental layout. The detector arms, mounted on a table, pivot to rotate around the target centre though angles up to 90° for Arm 1 and 70° for Arm 2. Because of space restrictions in the experimental area, a table which would allow rotation of the arms to angles greater than 90° could not be used. To make measurements at these angles the table was turned around and the beam refocussed on the new target position.

Negative pions cannot be recognised solely by dE/dX and total energy measurement as nuclear disintegration (star formation), on stopping, destroys the energy signature of the pion . The pion range, however, is a function of energy, and the elastically scattered pions may be separated by their range in a scintillator range telescope. The two range telescopes used (see Fig. 6) differed only in the elements that stopped the elastically scattered pions. The first two counters in each arm define the solid angle and select only particles coming from the direction of the target. The next thick counter almost stops the pions and defines the energy $\Delta E/\Delta X$. In Arm 1, the pions stop in the next counter, whose thickness is designed to

Figure 4. Beam Profiles.

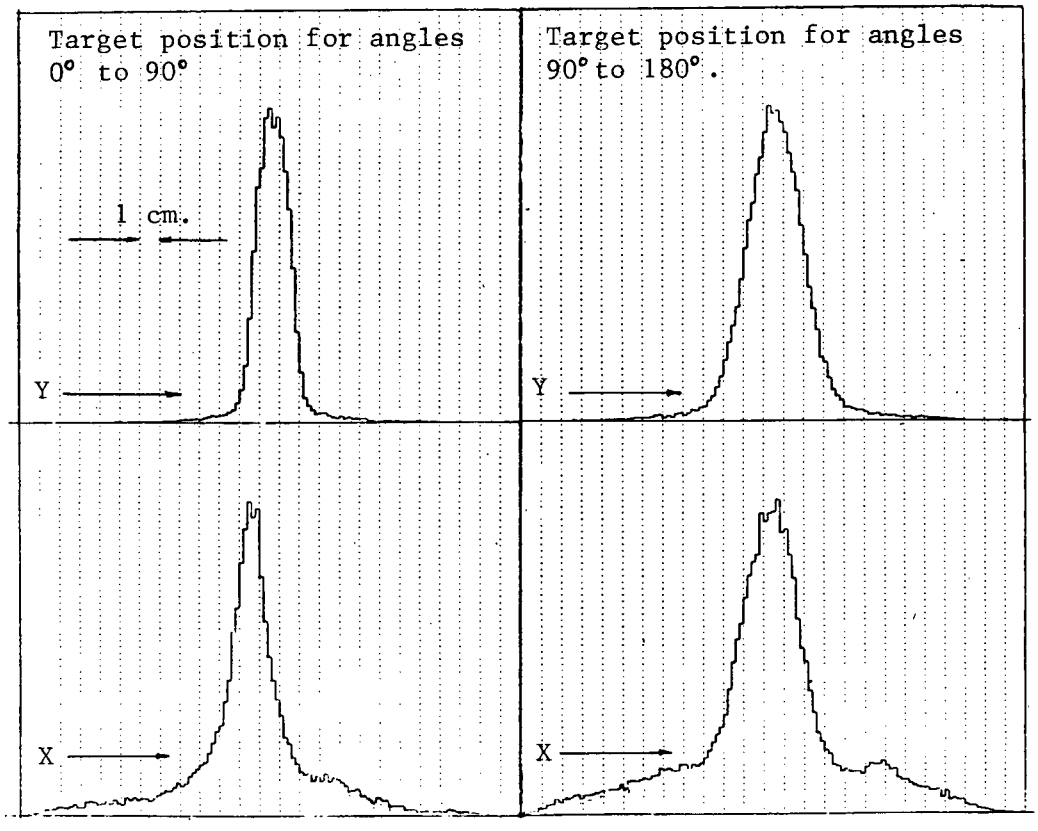

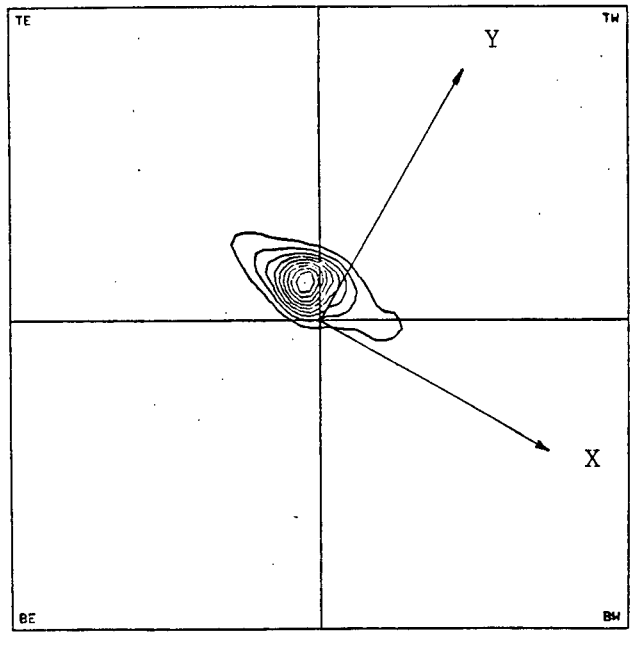

Contour plot of the beam at downstream target position

Figure 5. Experimental Layout.

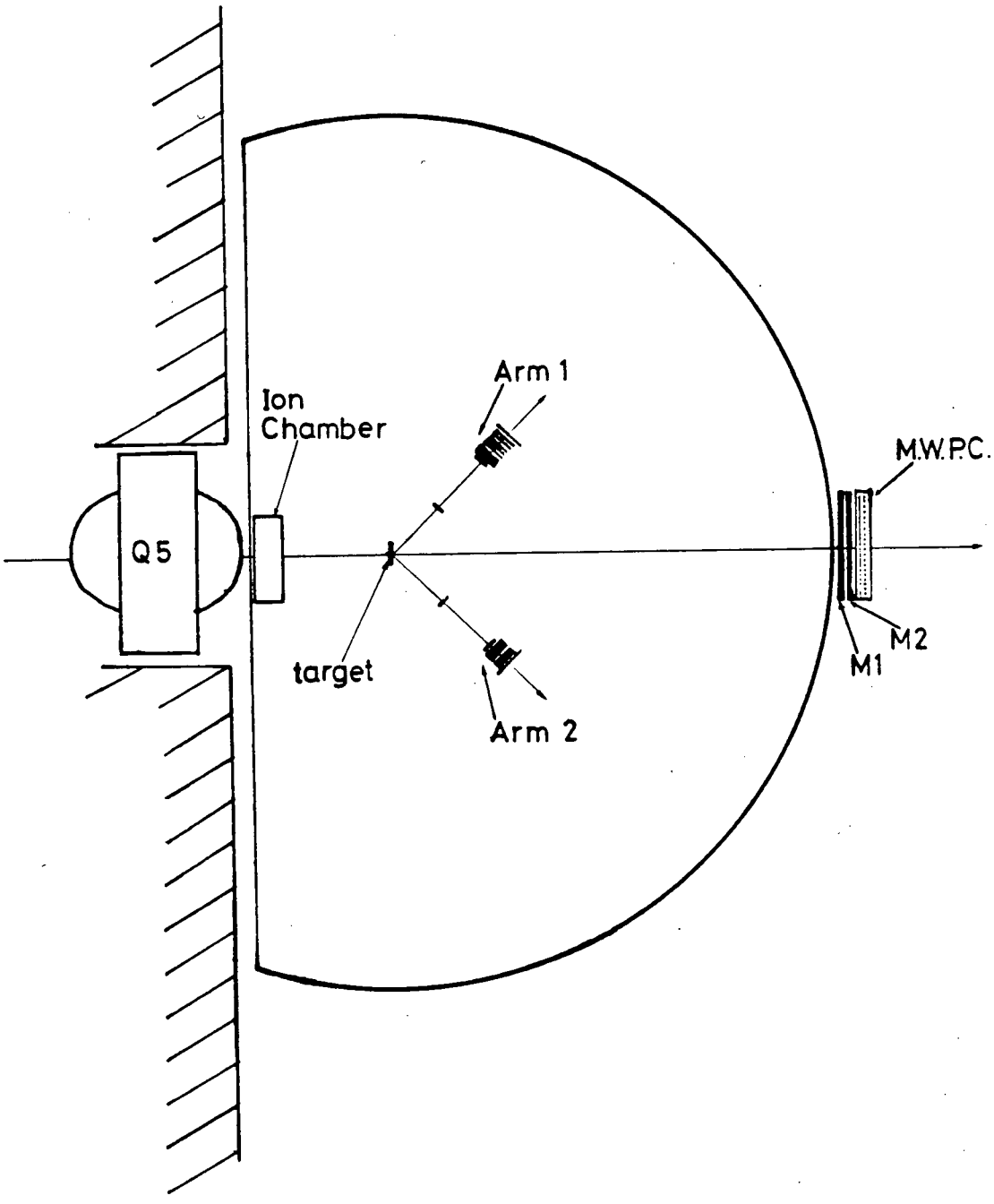

Figure 6. Range Telescopes.

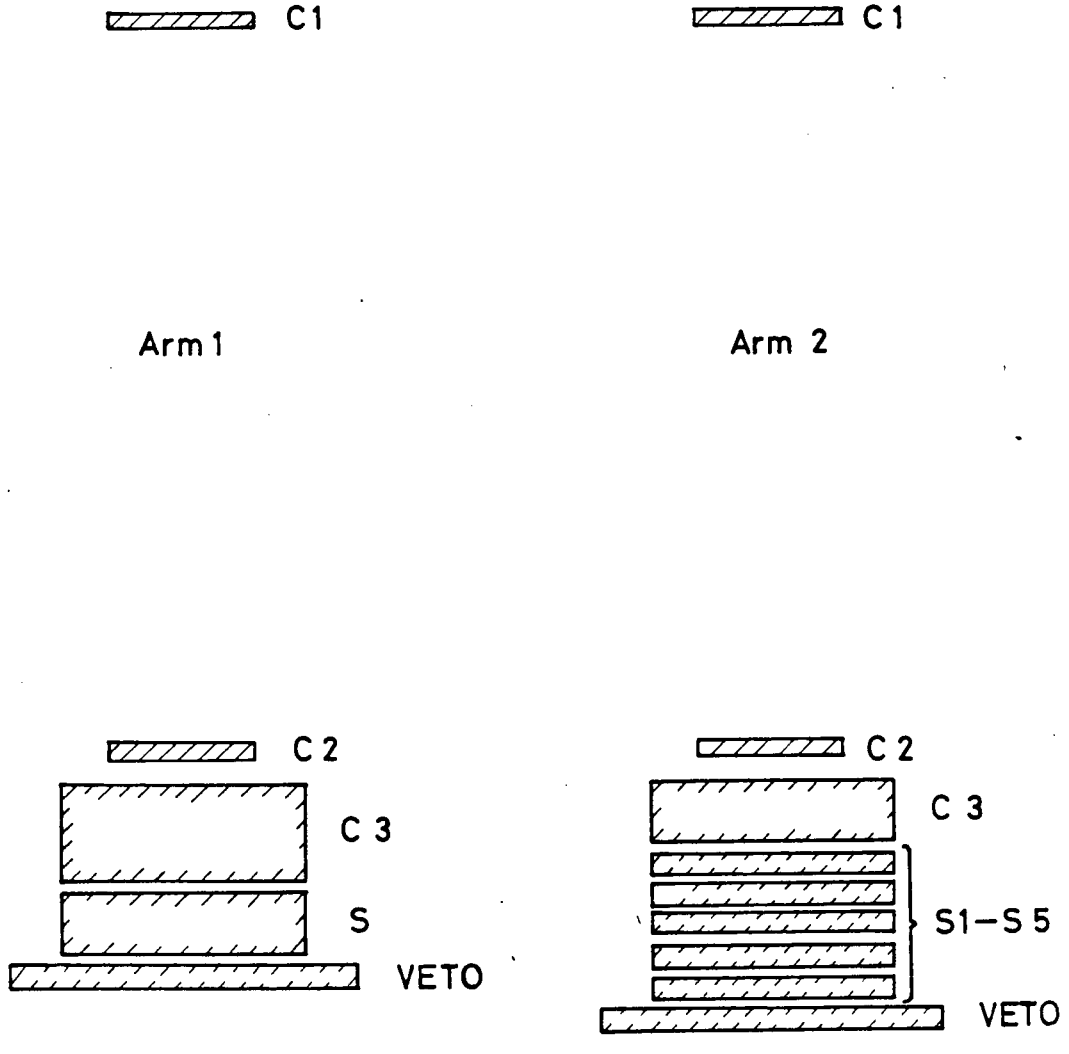

stop 28.4±3 MeV pions (30 MeV incident pion beam and 1.6MeV energy loss in the target). In Arm 2 this counter is replaced by five thin counters , the thickness of each being equivalent to approximately 1.9 MeV difference in pion energy. The final counter in each arm serves as a veto for particles that pass through the stack. The dimensions of the scintillators are given in Table II . The effective solid angles of the two telescopes were approximately 6 mb/sr (Arm 1) and 8 mb/sr (Arm 2).

The energy resolution is limited by the thickness of the stopping counters , range straggling, resolution of the incident beam and the energy spread caused by scattering from different depths in the target for some geometries. The contributions to the range distribution from these factors superimposed on the stopping counters , are shown in Fig. 7. The resulting stopping pattern, along with the experimental stopping pattern is shown in Fig. 8 . The convolution to combine the effects on the range distribution was done with a Monte-Carlo program[25] . A Gaussian shape was assumed for the range straggling with $\Delta r = .042 r_0$, where r_0 is the mean range. The ratio $\Delta r/r_0$ has been tabulated for protons over a wide energy range[26]. The corresponding values for pions may be evaluated from those of protons with the same range by accounting for the difference in masses of pions and protons $\Delta r/r_0$ for 30 MeV pions is found to be .032. Using $\Delta E = \Delta r \, \partial E/\partial r$ an intrinsic resolution of 1.2 MeV FWHM is obtained for the

---

See, for example, R. D. Evans, The Atomic Nucleus, pg. 664.

Table II. Dimensions of Scintillators in Telescopes.

ARM 1			ARM 2		
Counter	Diameter (cm)	Thickness (cm)	Counter	Diameter (cm)	Thickness (cm)
C1	3.0	0.33	C1	3.0	0.33
C2	3.0	0.33	C2	3.0	0.33
C3	5.0	1.97	C3	5.0	1.27
S	5.0	1.27	S1-S5	5.0X5.0	0.425
VETO	10.0X7.0	0.640	VETO	10.0X7.0	0.640

Figure 7. Range Distribution of Pions in Telescope.

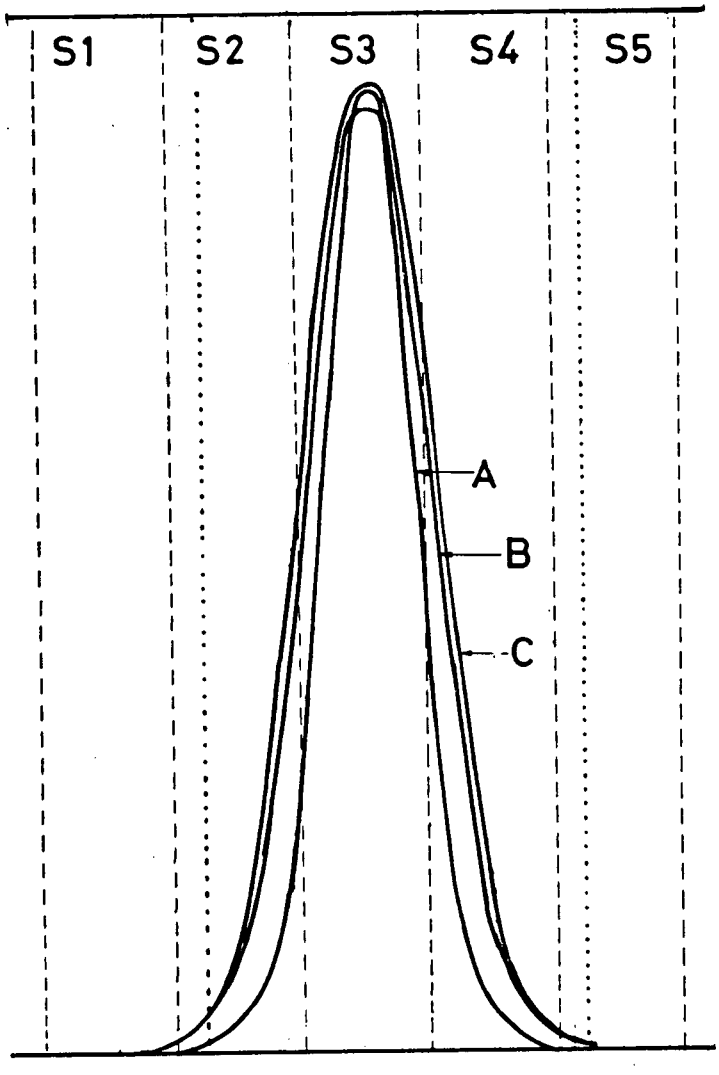

Range distributions including effects of

A Range straggling

B + 4.2% $\Delta p/p$

C + target thickness

Figure 8. Experimental and Calculated Stopping Patterns.

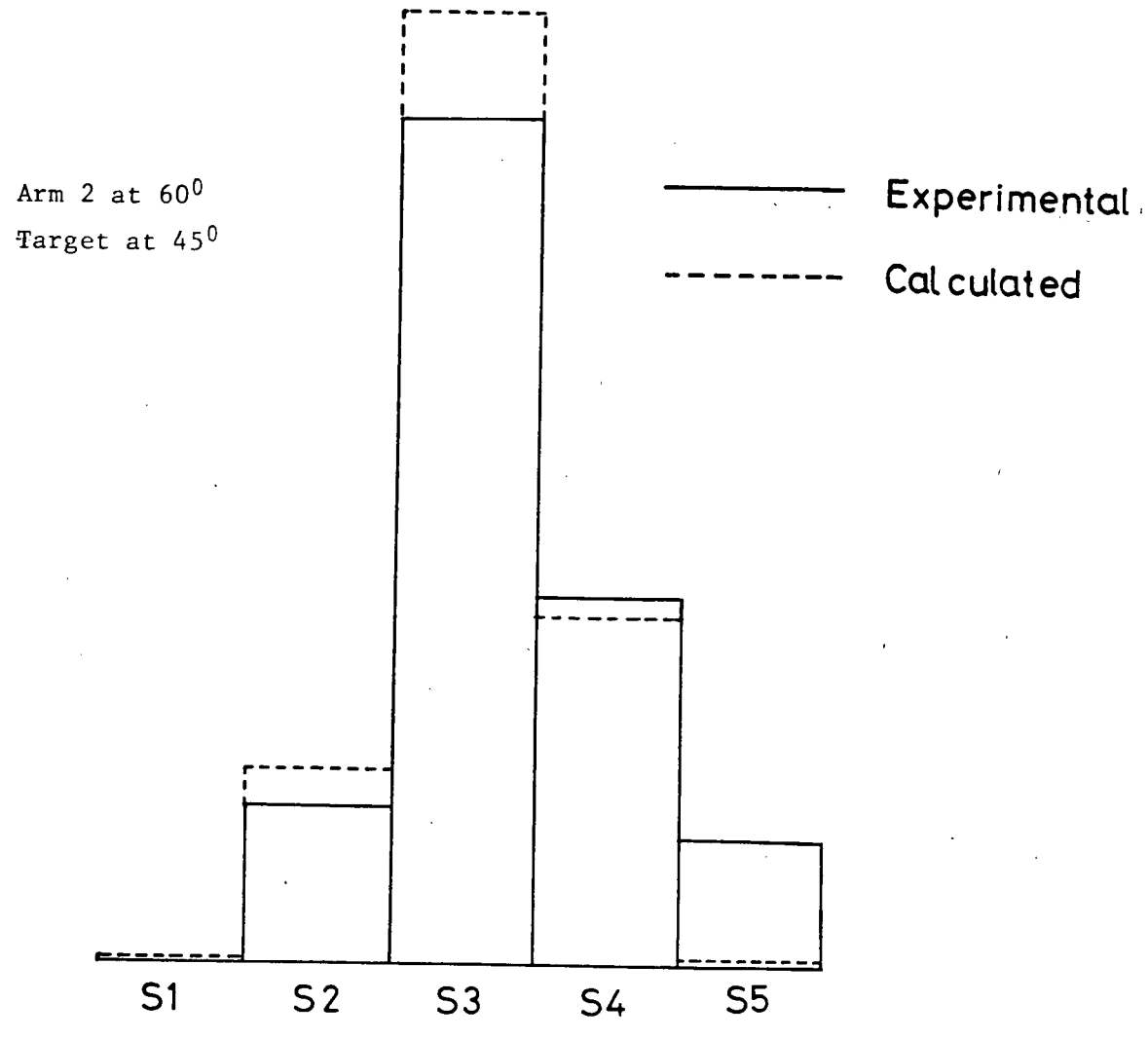

telescopes. Fitting to the stopping patterns of Arm 2 results in the value of $\Delta r/r_0 = .042$ used, corresponding to an intrinsic resolution of 1.6 MeV FWHM. Figure 9 compares the measured and calculated stopping patterns for 30MeV pions with $\Delta p/p = 4.2\%$ with the target in front of the telescope. The measured distribution has a long range tail caused by charged nuclear fragments from star formation travelling beyond the pion range, further limiting the resolution.

b) Targets

The ^{13}C and ^{12}C targets were made by compressing carbon powders into thin mylar frames. An empty frame was also made, the three frames being as similar as possible. The 5.17 cm. diameter circular rim of each target,of 0.019 cm. thick mylar, was 0.85 cm. deep and the two windows were of 0.00025 cm. thick mylar. The thickness of the windows represented less than 0.2% of the mass/cm.^{2} of the targets. Over 99% of the target frame mass was at the circumference, where the pion flux density was less than 5% of the peak.

The target density was limited by the requirement that the uncertainty in the pion energy on scattering be less than ±2 MeV. The area was then restricted by the amount (7gm.) of ^{13}C available. The target densities were .330 gm./cm.^{2} (^{13}C) and .327 gm./cm.^{2} (^{12}C). The ^{13}C target was of 99.7% isotopic purity while the ^{12}C target was of natural isotopic composition. Thin plastic holders were glued to the base of each target to allow precise relocation on the scattering table.

Figure 9. Experimental and Calculated Stopping Patterns at 0°.

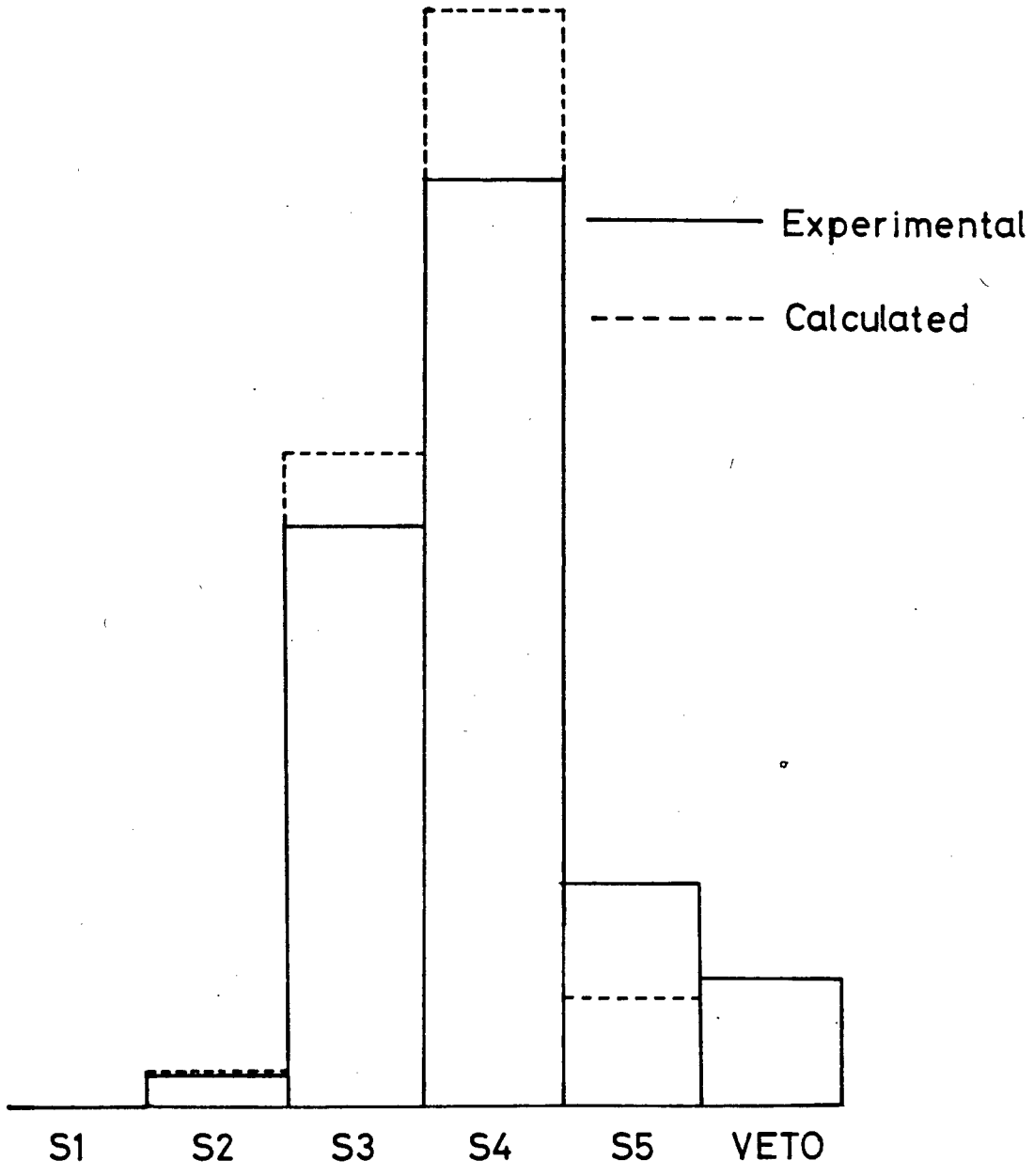

2. Experimental Procedure

Laser reference beams, which had previously been aligned by the biomedical group, were used to align our apparatus. Vertical and horizontal planar beams were aligned with their intersection along the beam direction and close to the beam centre. A 3" thick lead block with a 3/8" hole drilled through was placed at the target position with the hole along the laser beam intersection. A wire chamber profile of the beam just behind the lead was taken, clearly showing the position of the hole. The lead was removed and another profile taken so now the beam centre could be related to the laser intersection. The table and target were aligned using the laser system and aluminum blocks with relocating slots were fixed to the floor to provide automatic alignment if the table was moved. An additional check could be made on the table alignment with the beam direction using the approximate $1/\sin^4(\theta/2)$ dependence of the differential cross section at small angles. This is discussed in Chapter III.

A diagram of the electronic logic is given in Fig. 10. Many of the electrons were rejected by the discriminators, which were adjusted to accept all pions. In each arm an event was defined by the coincidence C1•C2•C3. The C2 counters were connected to constant fraction discriminators and the timing of the event was defined by the output pulse of this discriminator. The coincidence C1•C2•C3•RF, timed by the RF (the output pulse of the capacitive pickup), was used to start the TDC's, which were stopped by the event pulse C1•C2•C3, and also to interrupt the computer. Time-of-flight

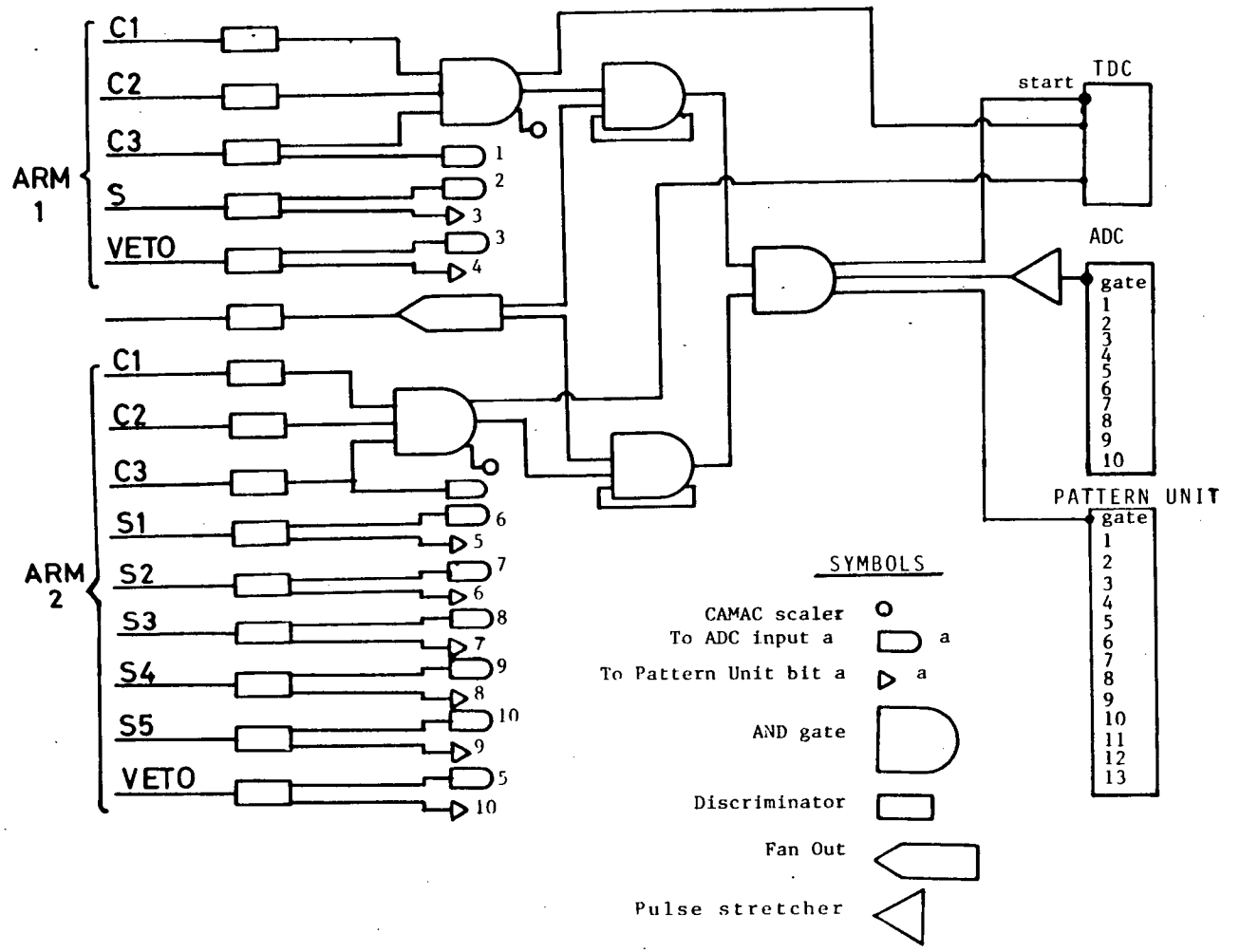

Figure 10. Electronic Logic.

and analogue signals were recorded for each event in CAMAC modules. Bits were set in a 24 bit C212 pattern unit for each element of the two arms which triggered in the event. The data were transmitted via a 2MHz serial CAMAC transmission link to a NOVA 1200 computer where they were buffered and then recorded on a magnetic tape. A real-time FORTRAN program interrogated the buffer and on command displayed time-of-flight, pulse height or stopping pattern information while the experiment was in progress.

Each angle involved runs with each of the two carbon targets and with the empty frame. Since the width of the stopping distribution depended on the target angle and the angle of scatter, the target angle was adjusted to the best compromise for the two arms. Each individual run was limited to less than 4 hours (mostly less than 2 hours) so that any long term drifts in detector efficiencies, ion chamber efficiency or pion fraction would not be appreciable in the time taken for the two carbon targets. Near the minimum of the cross section (60^{o}-70^{o}) the targets were interchanged until enough events were collected.

CHAPTER III

Analysis and Results

1. Analysis

A modified KIOWA histogramming routine on the UBC IBM 370 computer was used in the analysis of the data. Tests were made on each event and parameters of the event displayed on a histogram or scatterplot if the tests were successful. In this way cuts could be made on time-of-flight, energy deposited in C3 ($\Delta E/\Delta x$), energy deposited in the stopping counters (E), or the absence of a veto signal. A time-of-flight spectrum from Arm 1 (Fig. 11) shows the pions clearly separated from muons and electrons produced in the pion production target. The pion peak however contains protons from the carbon target and muons from pion decays between the target and detectors. Also at low angles ($\leq 40°$) many muons from pion decays in the beam are detected. These particles may be separated by cuts on the E and $\Delta E/\Delta X$ signals. The stopping counter is composed of 5 elements in arm 2 and the signals from these were added, weighted according to the relative gains. The relative gains were found from the signal strengths of the 96.3 MeV/c electrons from the channel. Since these have a range of 39 cm. in the scintillator they were assumed to deposit the same energy in each of the stopping elements.

Scatterplots of E vs. $\Delta E/\Delta X$ of particles in the pion time-of-flight peak were produced, with the coincidence requirement $C1 \cdot C2 \cdot C3 \cdot C4 \cdot \overline{VETO}$. Muons and protons were separated by cuts on $\Delta E/\Delta X$ (Fig. 12). Note that the pions have a well

Figure 11. Time-Of-Flight Spectrum from Arm 1.

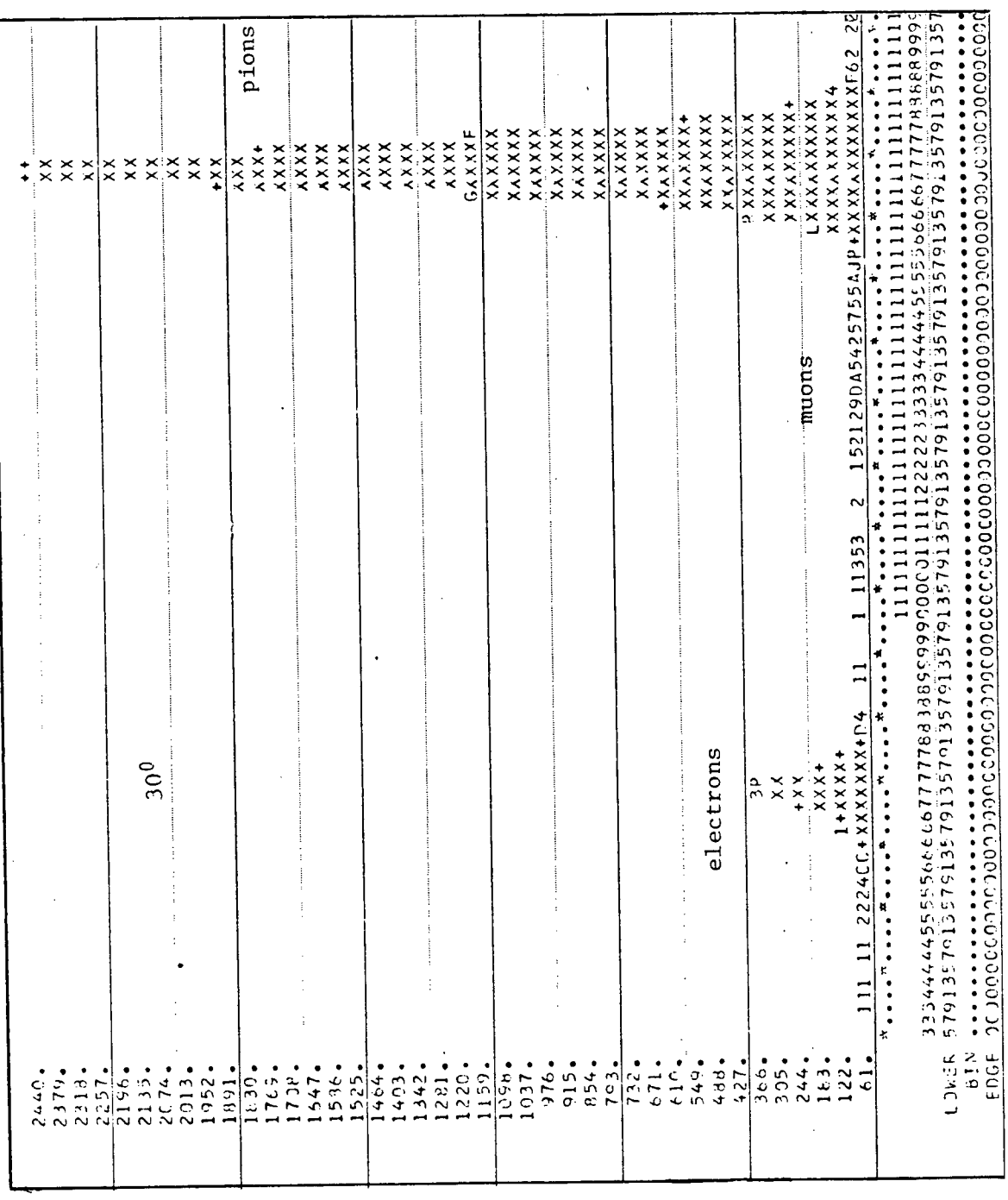

Figure 12. E vs. ΔE/ΔX Scatterplot Showing Cuts Made.

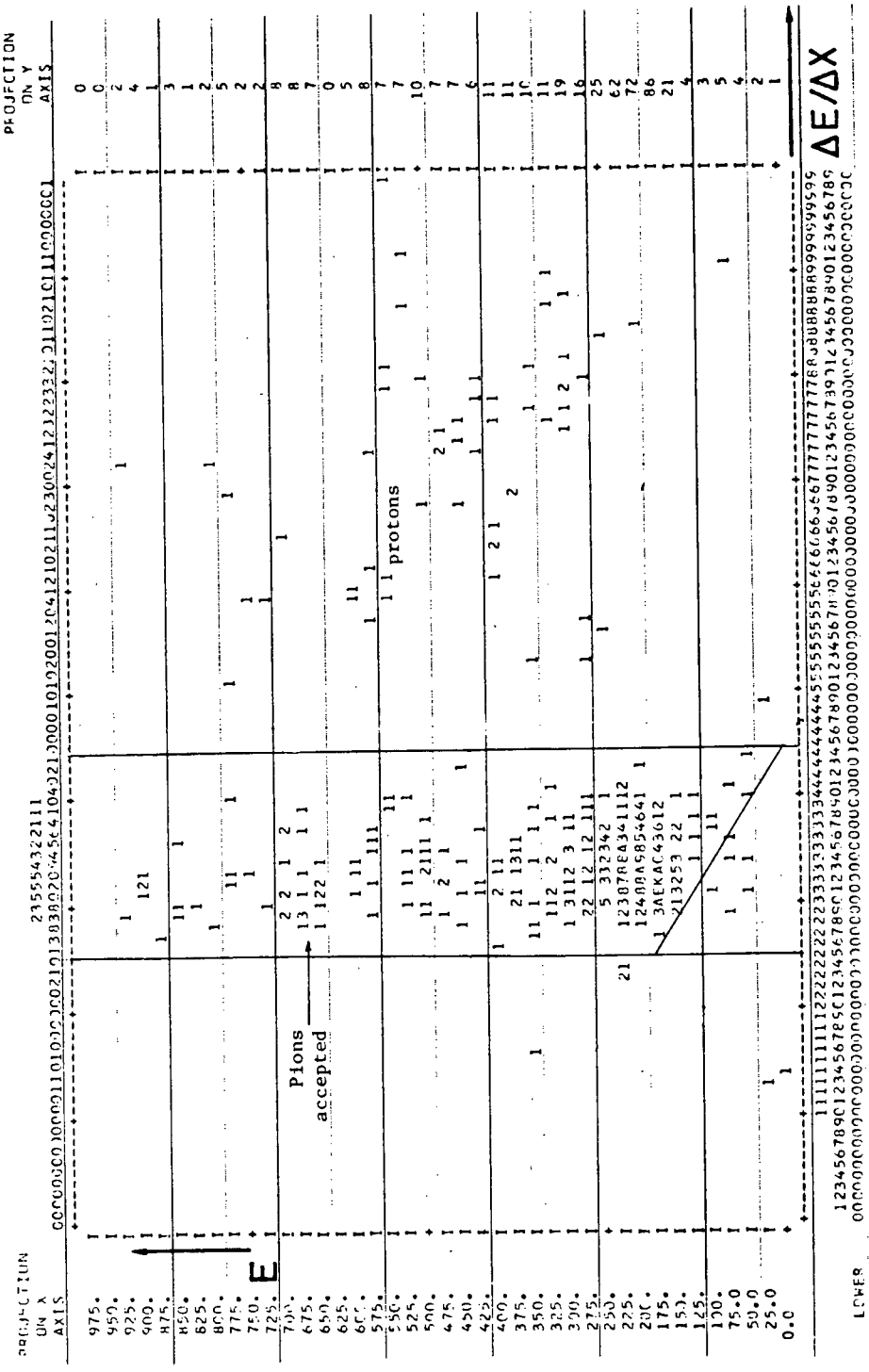

defined $\Delta E/\Delta X$ but a large spread in E, because of energy from nuclear disintegration on stopping. At angles less than 45° mucns from pion decay in flight are rejected by making a cut on E to include only picns producing nuclear disintegrations in the stopping counter (Fig. 13). The position of the cut to be made is found by examining the $\Delta E/\Delta X$ vs. E scatterplot of the empty target frame run which contains mostly muons at these angles.

In all cases the same cuts were made for ^{12}C, ^{13}C and empty target frame runs. The efficiencies of the detectors for detecting elastically scattered pions was the same for the three targets, assuming photomultiplier gains did not change appreciably during the time for the three runs.

Differential cross sections may be calculated from the data using

$$d\sigma/d\Omega = (N_F/IC_F - N_B/IC_B)\cos(\varnothing)\ SJ(\theta)/(F\Omega_{eff}\,DE_{\pi}T)$$

where

N_F and N_B are the number of pions detected during target in and target out runs,

IC_F and IC_B are the corresponding ion chamber readings,

F is a conversion factor from the ion chamber reading to the number of pions incident on the target,

$\varnothing$ is the angle between the target normal and the beam,

Ω_{eff} is the effective solid angle,

D is the fraction of pions reaching the detector from the target without decaying,

E_{π} is the efficiency of the detector arm for pions,

S is the fraction of the range distribution of the elastically

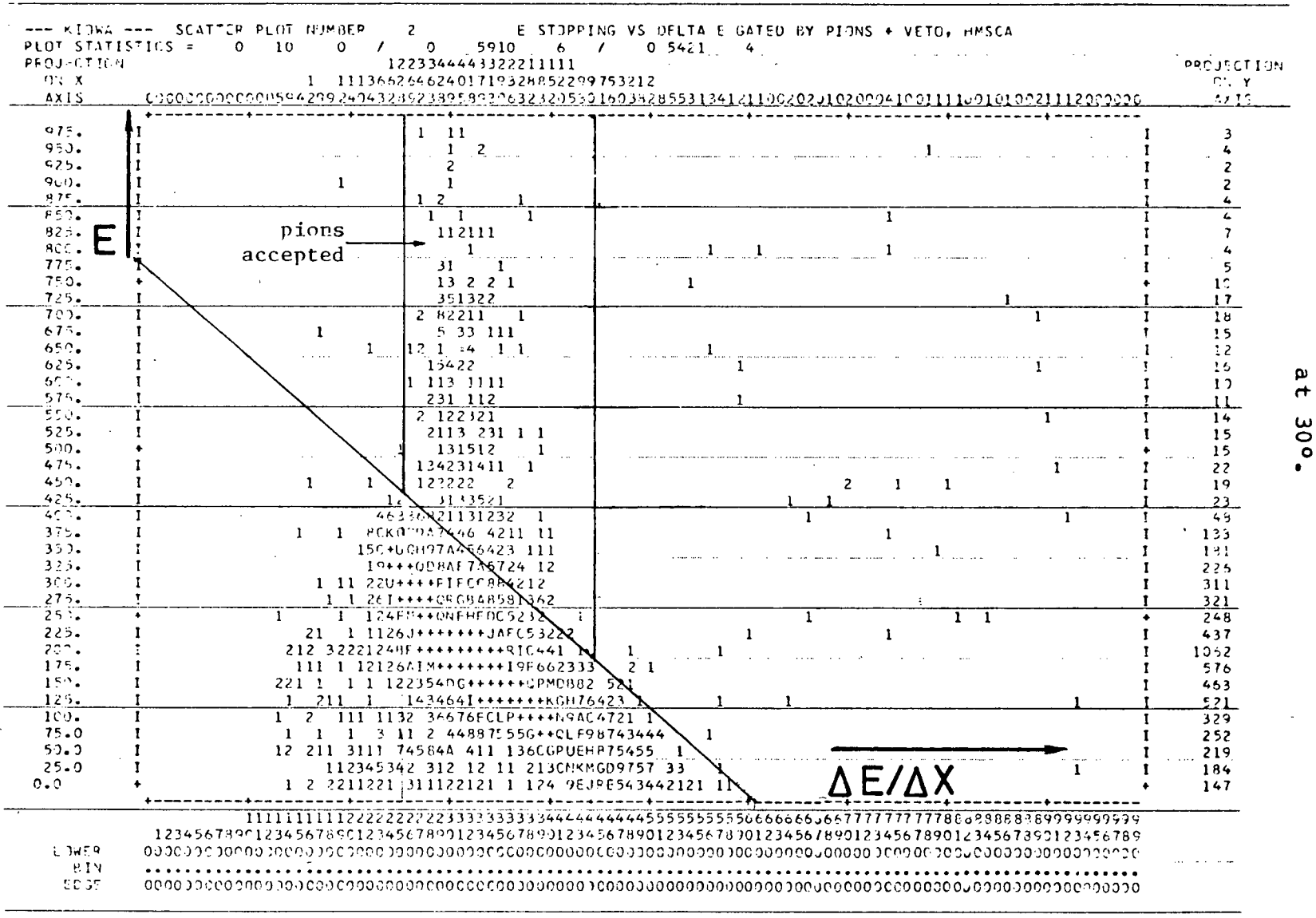

Figure 13. E vs. ΔE/ΔX Scatterplot at 30°.

scattered pions covered by the stopping element

$J(\theta)$ is the Jacobian $d\Omega_{lab.}/d\Omega_{c.o.m}$

T is the number of nuclei/cm² in the target.

In calculating the differential cross section ratio however most factors cancel , leaving

$$^{13}\sigma/^{12}\sigma = R = [\,^{13}N_F/^{13}IC_F - N_B/IC_B\,]/[\,^{12}N_F/^{12}IC_F - N_B/IC_B\,]\,^{12}T/^{13}T$$

Superscripts ^{12,13} signify quantities attributable to the run with ^{12}C, ^{13}C target respectively.

$J(\theta)$ is the same for ^{12}C and ^{13}C to better than 0.02% at all angles . Uncertainties in factors such as F , Ω_{eff} and E_π therefore do not affect the results.

Statistical errors were calculated from

$$\delta R/R = \{[\,\delta^{13}N_F\,\partial(\ln R)/\partial^{13}N_F\,]^2 + [\,\delta^{12}N_F\,\partial(\ln R)/\partial^{12}N_F\,]^2 + [\,\delta N_B\,\partial(\ln R)/\partial N_B\,]^2\}^{1/2}$$

$$= \sqrt{\frac{^{13}N_F}{^{13}IC_F\left[\frac{^{13}N_F}{^{13}IC_F} - \frac{N_B}{IC_B}\right]^2} + \frac{^{12}N_F}{^{12}IC_F\left[\frac{^{12}N_F}{^{12}IC_F} - \frac{N_B}{IC_B}\right]^2} + IC_B\frac{N_B\left[\frac{^{13}N_F}{^{13}IC_F} - \frac{^{12}N_F}{^{12}IC_F}\right]^2}{\left[\left(\frac{^{13}N_F}{^{13}IC_F} - \frac{N_B}{IC_B}\right)\left(\frac{^{12}N_F}{^{12}IC_F} - \frac{N_B}{IC_B}\right)\right]^2}}$$

where δx signifies the statistical error in x.

Where more than one set of runs had been taken at one angle the statistically weighted mean of the ratios was calculated. In all such cases the distribution of values for the ratio was consistant with statistical errors.

The angle of the beam relative to the 0° line of the

scattering table was evaluated from three pairs of runs with the same arm and target at 30° left and 30° right . Assuming the cross section at 30° varies as $1/\sin^4(\theta/2)$ from Rutherford scattering, then the ratios of left and right cross sections may be written

$$\sigma(\theta-C+X)/\sigma(\theta-C-X)=\sin^4((\theta-C-X)/2)/\sin^4((\theta-C+X)/2)$$

C= the correction to the mean scattering angle for finite solid angle (see below).

X= the angle between the beam direction and 0° on the scattering table.

Writing $\theta-C$ as θ_c and left, right differential cross sections as σ_L, σ_R respectively one gets

$$[\sigma_L/\sigma_R]^{1/4}=\sin[(\theta_c-X)/2]/\sin[(\theta_c+X)/2]$$

$$=[\sin(\theta_c/2)-\cos(\theta_c/2)\,X/2]/[\sin(\theta_c/2)+\cos(\theta_c/2)\,X/2]$$

$$\therefore\quad X=[2\sin(\theta_c/2)/\cos(\theta_c/2)][1-(\sigma_L/\sigma_R)^{1/4}]/[1+(\sigma_L/\sigma_R)^{1/4}]$$

σ_L/σ_R is evaluated in the same way as R. Three values of X (0.43, 0.61, 0.37) are obtained from three 30° left, right runs, giving X= 0.5°±.1° where the error is simply the standard deviation of the three values. The angle X is added to all the angles for arms on the left and subtracted from those on the right. An additional problem remains in defining the mean scattering angle over the detector at small angles, since the differential cross section varies rapidly and non-linearly here. The mean scattering angle should be evaluated by

averaging the distribution of scattering angles produced by the finite beam spot size and solid angle subtended by the detectors, weighting each angle with the cross section at that angle, or to a good approximation by $1/\sin^4(\theta/2)$. Since, however, the ratio of cross sections does not vary rapidly in this region , the correction was only evaluated approximately by considering a point beam spot. The integration was then performed cver the second detector which defines the solid angle for a point source. The results for 30° and 40° are 29.6° and 39.8.

Because of the broadening of the range distribution and the inherent width due to range straggling it is possible for inelastically scattered pions to be detected in the stopping counters. The efficiencies for detecting the pions from the 4.4 MeV state of ^{12}C and the 3.68 MeV state of ^{13}C were evaluated using the Monte Carlo program mentioned previously to simulate the two arms . The cross sections for the elastic scattering and to these excited states were calculated by E. Rost[27]. The small efficiencies combined with a small ratio of inelasic to elastic cross section and a tendency for the inelastic contributions to cancel in the ratio all contrive to give a very small effect. An estimate of the size of the inelastic contribution to R was made for large angles where the ratio σ(inelastic)/σ(elastic) is greatest. The results are shown in Table III.

2. Results

The differential cross section ratio results for each set of runs and the weighted means for each angle are given in Table IV. In cases where two angles were very close ($\leq 1^{o}$) the ratios were combined by evaluating the weighted mean and weighting the angles similarly to find the mean angle (Table V and Figure 14). The results in Table V were used in the analysis discussed in the following sections.

Table III. Inelastic Scattering Contribution to R.

Angle	^{12}C Cross Sections (mb/sr)		^{13}C Cross Sections (mb/sr)		E^{12}	E^{13}	R/R′
	Elastic	4.4MeV	Elastic	3.68MeV			
130	8.4	0.49	11.6	0.40	.61	.34	.998
140	9.1	0.62	12.5	0.49	.59	.34	1.00
150	9.6	0.73	13.1	0.57	.62	.36	1.00

E^{12} and E^{13} are the ratios of the efficiencies for elastic/inelastic scattering of ^{12}C and ^{13}C.

R′ = the measured ratio with no correction for inelastic scattering.

Table IV. Results.

Angle c.o.m	$^{136}/^{126}$ (R)	Weighted Mean
29.5	0.953±.093 0.971±.065	0.965±.054
30.5	1.018±.10	
39.5	1.052±.065 0.888±.041	0.935±.035
45.0	0.931±.041	
50.1	0.985±.066	
60.2	1.245±.093	
61.2	1.263±.126	
66.2	1.64 ±.22 1.81 ±.35 1.34 ±.16 1.53 ±.13	1.511±.089
70.3	1.59 ±.32 1.59 ±.22	1.59 ±.18
71.3	1.63 ±.12	
80.3	1.83 ±.14 1.70 ±.13 1.79 ±.14	1.77±.11
85.3	1.46 ±.10	
90.4	1.47 ±.11 1.427±.084	1.442±.066
91.4	1.46 ±.11 1.37 ±.13	1.421±.084

Table IV. (continued)

Angle c.o.m	$^{13}\sigma/^{12}\sigma$ (R)	Weighted Mean
100.5	1.58 ±.13 1.56 ±.13	1.575±.094
111.3	1.217±.073	
115.2	1.222±.061	
131.1	1.281±.069	
141.1	1.098±.064	
149.9	1.134±.090	
150.9	1.26 ±.13 1.153±.064	1.175±.057

Table V. Elastic Scattering Cross Section Ratios of $^{13}C/^{12}C$.

Angle c.o.m.	$^{13}6/^{12}6$ (R)
29.8	0.976±.047
39.8	0.935±.035
45.0	0.931±.041
50.1	0.985±.066
60.6	1.252±.075
66.2	1.511±.089
71.0	1.61 ±.10
80.3	1.77 ±.079
90.7	1.434±.052
101.3	1.575±.094
110.3	1.217±.073
115.2	1.222±.061
130.5	1.281±.069
140.5	1.098±.064
150.6	1.163±.048

Figure 14. Elastic Scattering Cross Section Ratios of $^{13}C/^{12}C$.

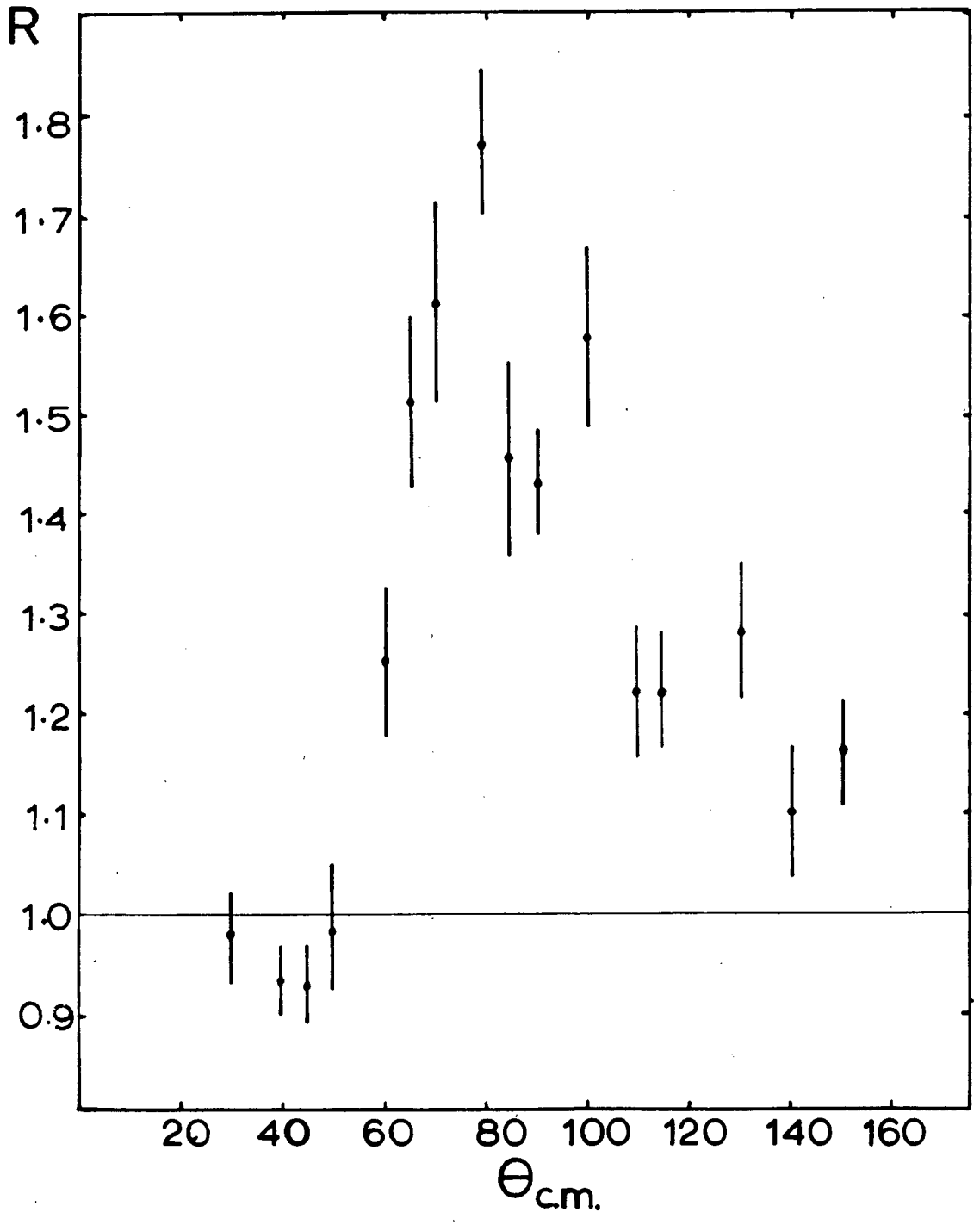

CHAPTER IV

Theoretical Interpretation

It can be seen immediately from Fig. 14 that the π^- is more sensitive to the effects of the valence neutron in ^{13}C than is π^+ at 50 MeV. (Fig. 1) . The large peak centred at 70°-80° is due to a change in the structure in the s-p interference minimum between ^{12}C and ^{13}C. The elastic scattering differential cross section[28] of 29 MeV π^- on ^{12}C is shown in Fig. 15 together with the results of an optical potential calculation (see section 2). Multiplying the optical potential calculation by the values of R in Table V gives the line indicated. It can be seen that the minimum of the ^{13}C cross section has been shifted slightly and raised above that of ^{12}C.

1. Point Nucleus Impulse Approximation Model

A simple calculation was made to see how far this structure is predicted by the pion-nucleon amplitudes. The ratio of cross sections was evaluated by adding together the scattering amplitudes of the twelve nucleons for ^{12}C and adding the extra n-n amplitude for ^{13}C. This gives for the ratio

$$R=[\,13b_o+b_1+(13c_o+c_1)\,k^2\cos(\theta)\,]^2/[\,12b_o+12c_o\,k^2\cos(\theta)\,]^2$$

where $k=.48$ fm^{-1} for 30 MeV pions

Optical potential parameters b_o , b_1 , c_o and c_1 were used rather

Figure 15. Comparison of ^{13}C and ^{12}C Differential Cross Sections.

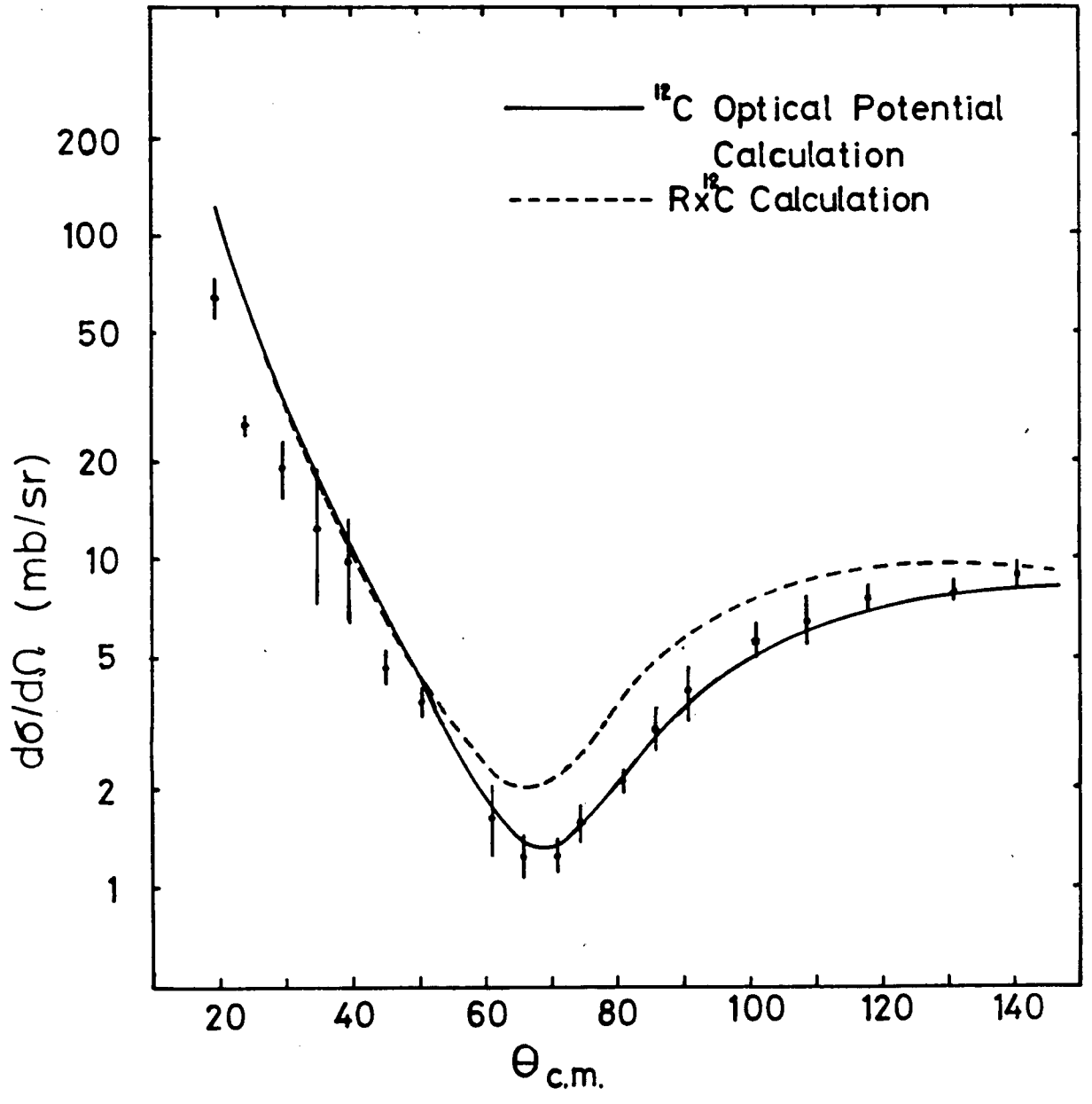

than free πN amplitudes to give a better approximation to scattering in the nucleus. The main difference is in an increase in b_o. The parameters were taken from Stricker, McManus and Carr[5], (SMC), Set 1 (Table VI, Set B). Imaginary terms were added to b_o and c_o. The imaginary terms were

$$\text{Im } b_o = .020 \text{ fm.}; \quad \text{Im } c_o = .047 \text{ fm}^3$$

The sizes of the imaginary terms were chosen to give approximately the correct value for R at 80°, but the relative sizes of Im b_o and Im c_o were taken from the ratio of the imaginary parts to the s and p wave annihilation strengths of SMC Set 1.

The result is shown as the dashed line in Fig. 16. The maximum is predicted at the correct position and the trend at large angles is roughly correct. At low angles, however, the agreement is not good, although the dip below R=1 is predicted. The same calculation with imaginary terms set to zero is also shown (dotted line). By increasing the absorption the dip is greatly reduced since now the cross section minimum of ^{13}C is not only shifted in angle but is also raised by the imaginary terms. The imaginary terms are such that the s-p interference minimum becomes less deep as it is moved to a smaller angle. Since this model essentially uses a point nucleus, one would expect the relative amounts of s and p waves to differ from those of a finite size nucleus. Also multiple scattering in the nucleus may have the effect of reducing the p-wave scattering, by the Lorenz-Lorentz effect. Reducing the p-wave amplitude by proportionaly the same amount in both nucei, by simply changing k to .32 fm^{-1} , produces the solid curve. This curve represents

Figure 16. Impulse Approximation Calculations of R.

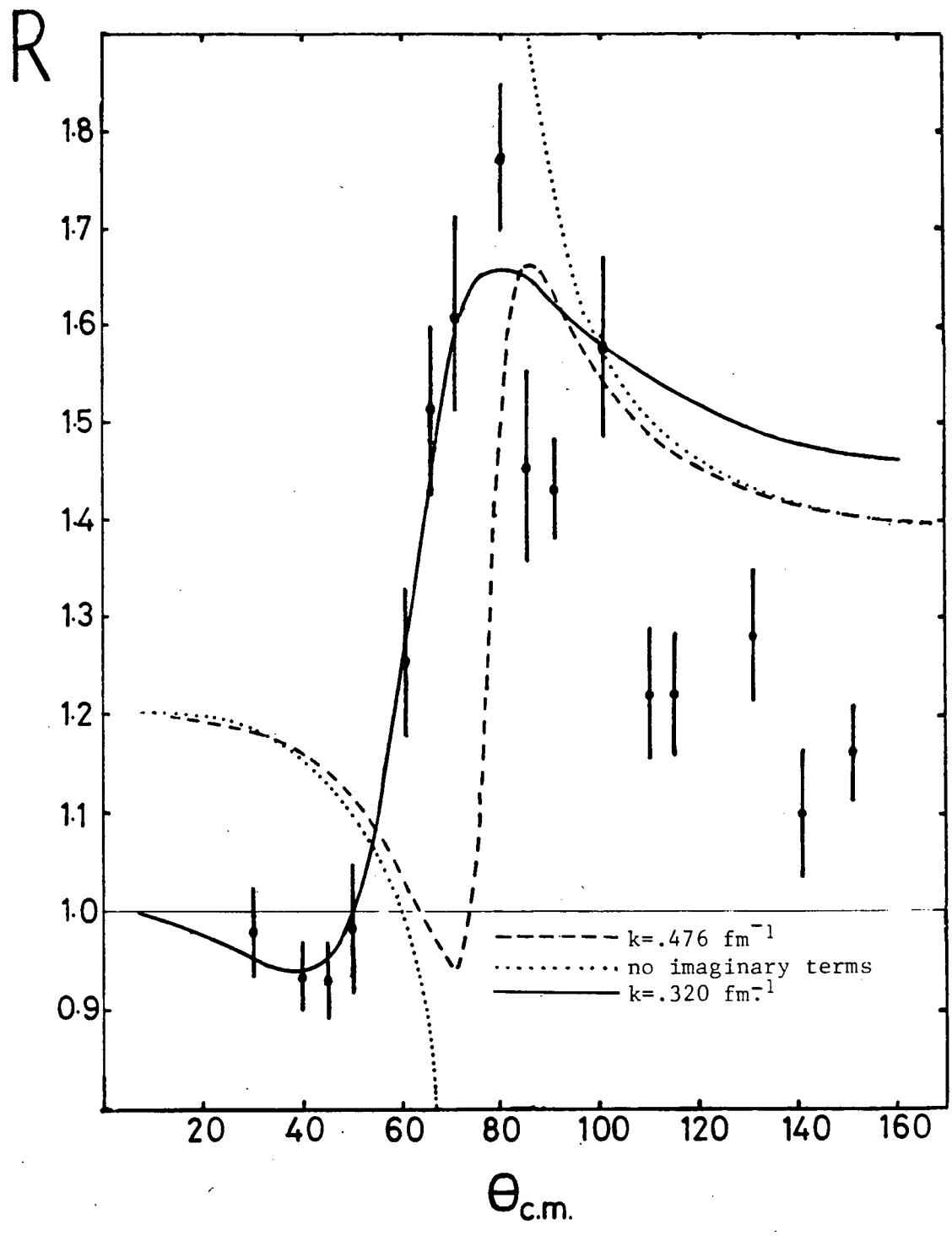

the best fit to the data when only k is varied. All the essential features of the distribution of R can be seen in this curve although quantitatively the agreement is not good. The same calculation for 50 MeV π^+ with k reduced by the same factor is shown in Fig. 1. Again qualitatively the agreement is quite good and it is seen that the smaller size of the ratio near the cross section minimum is due to the minimum being shifted by a smaller amount and in the opposite direction than in the 30 MeV π^- case. The imaginary terms then produce a decrease in the cross section which is cancelled partly by the increase in number of nucleons.

Such reasonable qualitative agreement using so simple a model suggests that calculations using an optical potential incorporating the correct kinematics and finite size effects should be reliable !

2. Optical Potential Calculations

The optical potential used was that of Stricker, McManus and Carr[5] and was of the form

$$2\bar{w}U_{opt} = -4\pi\{b(r) + p_2 B_0 \rho^2(r) + (c_0(p_1 - 1)/2p_1 \nabla^2 \rho(r))$$
$$+ [c_0(p_2 - 1)/2p_2] \nabla^2 \rho^2(r)\}$$
$$+ 4\pi[\underset{\sim}{\nabla} \cdot L(r) c(r) \underset{\sim}{\nabla} + c_0/p_2 \underset{\sim}{\nabla} \cdot \rho^2(r) \underset{\sim}{\nabla}] + 2\bar{w}V_c(r)$$

where

$b(r) = p_1 (b_0 \rho(r) - \varepsilon_\pi b_1 \delta\rho(r))$

$c(r) = 1/p_1 (c_0 \rho(r) - \varepsilon_\pi c_1 \delta\rho(r))$

$\delta\rho(r) = \rho_n(r) - \rho_p(r)$

$\varepsilon_\pi = -1$ for π^- and $+1$ for π^+

$L(r) = (1 + 4\pi\lambda(A-1)c(r)/3A)^{-1}$ is the Ericson-Ericson factor

V_C = Coulomb potential

$\bar{w}=w/(1+E/A)$ is the pion reduced energy, where w is the pion total energy in the pion-nucleus centre of mass frame, $E=w/M$ and M=nuclear mass/A.

The factors

$$p_1 = (1+E)/(1+E/A)$$

and

$$p_2 = (1+E/2)/(1+E/A)$$

are reduced mass factors.

The terms involving $\nabla^2\rho$ and $\nabla^2\rho^2$ are to account for transformation from the πN centre of mass system to the πA system[29]. This potential is described fully in SMC.

The wave equation used to calculate the elastic scattering cross sections was of the form

$$(\nabla^2+k^2+2wU_{opt})\phi(r)=0$$

where k is the wave vector of the pion-nucleus centre of mass system. A program developed by A. Thomas and M. Krell was used to evaluate the partial wave phase shifts and hence the differential cross sections from the wave equation.

The set of optical potential parameters used (set A, Table VI) was taken from SMC set 1, with the absorption parameters, B_0 and C_0, adjusted to fit the ^{12}C differential cross section (Fig. 17). The data[28] in Fig. 17 are the combined results of several runs. The real and imaginary parts of B_0 and C_0 were kept equal in accordance with pionic atom data[4].

A modified Gaussian form,

$$\rho(r)=\rho_0[\ 1+\alpha(r/a)^2\ ]\exp[-(r/a)^2]$$

where ρ_0 =nucleon density at the centre, was used for the proton

Table VI. Optical Potental Parameters.

	SET A	SET B	SET C	Units
b_0	-.040+i.002	-.040+i.002	-.040+.002	fm.
b_1	-.11 -i.001	-.11 -i.001	-.11 -i.001	fm.
B_0	-.17 +i.17	-.13 +i.13	-.17 +i.17	$fm.^4$
c_0	.75 +i.007	.75 +i.007	.75 +i.007	$fm.^3$
c_1	.62 +i.004	.62 +i.004	.62 +i.004	$fm.^3$
C_0	-.79 +i.79	-.75 +i.75	-.79 +i.79	$fm.^6$
λ	1.0	1.0	0.6	

Figure 17. Calculations of ^{12}C Cross Section with Parameter Sets A, B and C.

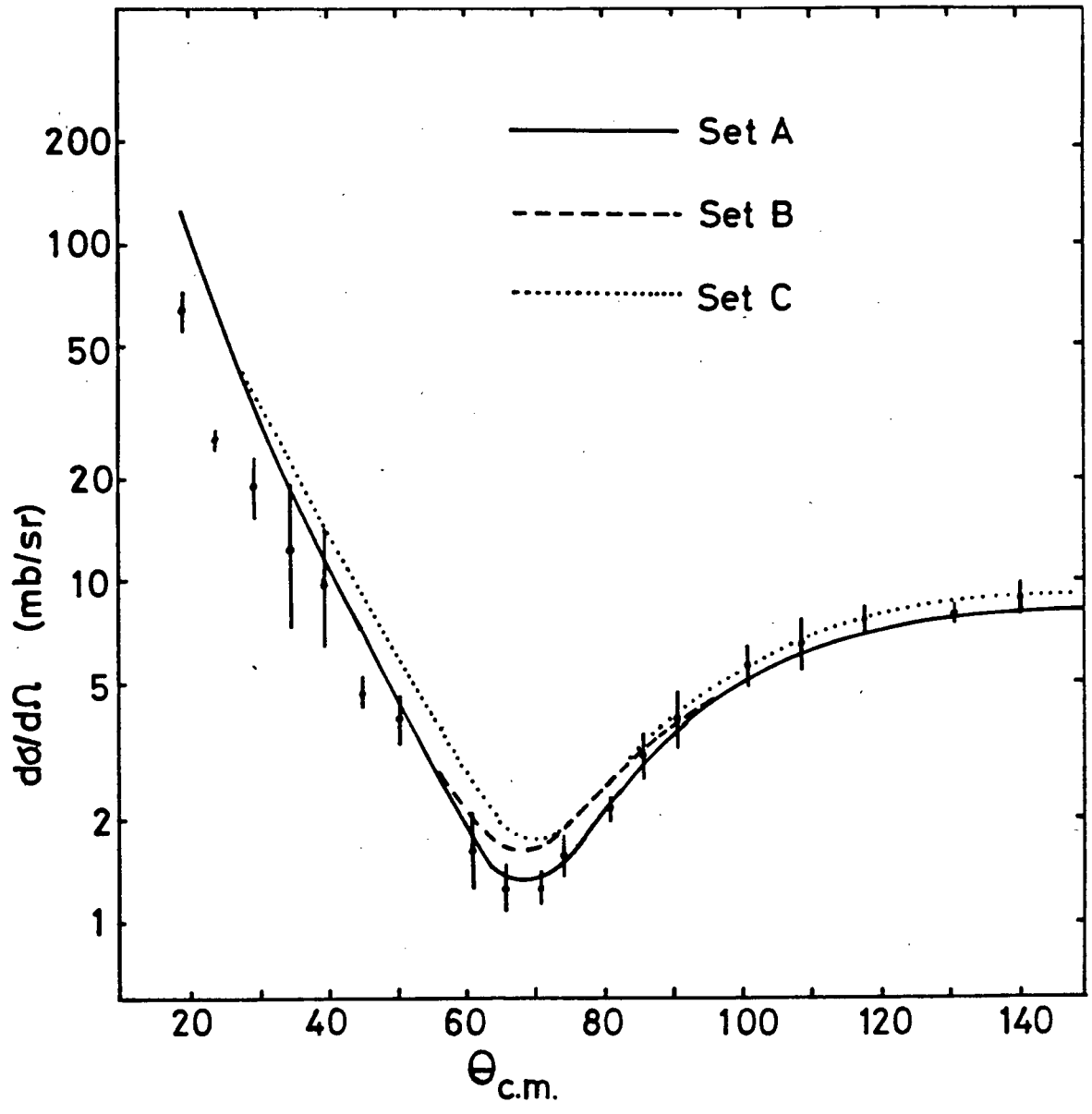

and neutron distributions of ^{12}C. The parameter , α , was set to the shell model value,

$$\alpha = (Z, N-2)/3$$

for neutron , proton distributions. The rms. radius is then given by

$$\langle r^2_{p,n} \rangle^{1/2} = \left[\; 2.5-2/Z,N \; \right]^{1/2} a$$

The proton rms. radii, r_p , were obtained by subtracting out the proton size from the charge radii, $\langle r_c^2 \rangle^{1/2}$ given by electron scattering, using

$$\langle r_p^2 \rangle = \langle r_c^2 \rangle - .8^2$$

The neutron and proton distributions for ^{12}C were assumed equal as is reasonable from their closed shell nature and from Hartree-Foch calculations[16]. The charge radius[30] of ^{12}C, $^{12}r_c = 2.46 \pm .025$ fm., gives proton and neutron radii of $^{12}r_{p,n} = 2.326 \pm .026$ fm.

There is some discrepency in the literature on the rms. charge radius of ^{13}C. The ratio of $^{13}C/^{12}C$ rms. charge radii was measured to be $.96 \pm .01$ by Crannell[31] et al. at Stanford. The momentum transfer range covered in the experiment was .7 to 1.7 fm^{-1}. Yang et al. at Saskatoon[32] later measured the ratio tc be $.975 \pm .02$, covering the momentum transfer range of .2 to 1.1 fm^{-1}. They combined the two results to give a ratio of $.968 \pm .015$. In a higher energy electron scattering experiment Heisenberg et al.[33] found a ratio of $.9907 \pm .0004$. They attribute the discrepency with the results of Cranell as being due to the difficulty in determining the target thickness with the low purity liquified methane target used by Cranell. This is suggested by the difference in cross section ratios of

$^{13}C/^{12}C$ measured by the two experiments at the same momentum transfer. Yang used a gas methane target, enriched to 84%. The high momentum transfer result , $^{13}r_c = 2.44$ fm., has been used in this analysis, but checks are made of the dependence on the proton radius.

Two different approaches were used to describe the ^{13}C neutron distribution . Firstly the density distribution of a neutron with a p-wave harmonic oscillator wavefunction was added to the Gaussian distribution of a 6 neutron core. Sensitivity to the size of the neutron core was investigated. In the second case a modified Gaussian distribution was used for the 7 neutrons and a determination of the neutron rms. radius of ^{13}C was made.

Since the point at 100° must be in disagreement with any reasonable fit, this point was left out of the χ^2 evaluations so that it would not effect the positions of χ^2 minima. The different calculations, however, tended to converge at this point so the influence on the χ^2 minima would not be great.

a) Core + Valence Neutron Model

The wave function of the p-wave neutron was averaged over all angles. The harmonic oscillator well strength, ν, was left as a parameter to be varied. The wavefunction of a particle in a spherical harmonic well is given by

$$\phi_{n\ell m}(r) = R_{n\ell}(r)\ Y_\ell^m(\theta)$$

where n is the number of internal radial nodes and l is the angular momentum quantum number.

$$R_{nl}(r)=\sqrt{\frac{\nu^{3/2}2^{l-n+2}(2n+2l+1)!!}{\sqrt{\pi}\,n!\,((2l+1)!!)^2}}\;(\nu r^2)^{l/2}\;L^{l+1/2}(\nu r^2)\,e^{-\nu r^2/2}$$

and

$$L^{l+1/2}(\beta)=\sum_{k=0}^{n}(-1)^k\,2^k\binom{n}{k}\frac{(2l+1)!!}{(2l+2k+1)!!}\,\beta^k$$

$\nu=m\omega/\hbar$, where m= the reduced mass and ω = the oscillator frequency.

For the p-wave neutron of ^{13}C, n=0, l=1. The rms. radius is given by

$$\langle nl|r^2|nl\rangle=(2n+l+3/2)\nu^{-1}=5/2\nu$$

For the 6 neutrons of ^{12}C the rms. radius is then

$$[(2x3/2+4x5/2)/6\nu]^{1/2}$$

assuming a harmonic well. For an rms. radius of 2.326 fm. the well depth, ν, for ^{12}C is .40 fm^{-2}. It might be expected that the effective well depth for the extra neutron of ^{13}C will be smaller than this since the neutron is unpaired.

Using equal neutron and proton distributions of rms. radius= 2.306 fm. for the core of ^{13}C (reduced core) calculations of R were made for varying well strength, ν. The calculations were repeated for ^{13}r =2.306 fm and neutron core radius of 2.326 fm. (equal to ^{12}C radius). The best fits in the two cases were essentially identical, (Fig. 18) and the agreement with the data is good, except perhaps for small angles. The χ^2 for the best fits are the same , although the minimum is sharper for the reduced core case (Fig. 19). Also shown in Fig. 19 is the χ^2 curve for a neutron core radius of 2.360 fm. It can be seen that as the core radius increases the best fit well strength increases. The χ^2 curves are generally not parabolic. The positions of the minima are therefore

Figure 18. Optical Potential Calculations of R. Valence Neutron + Core Model.

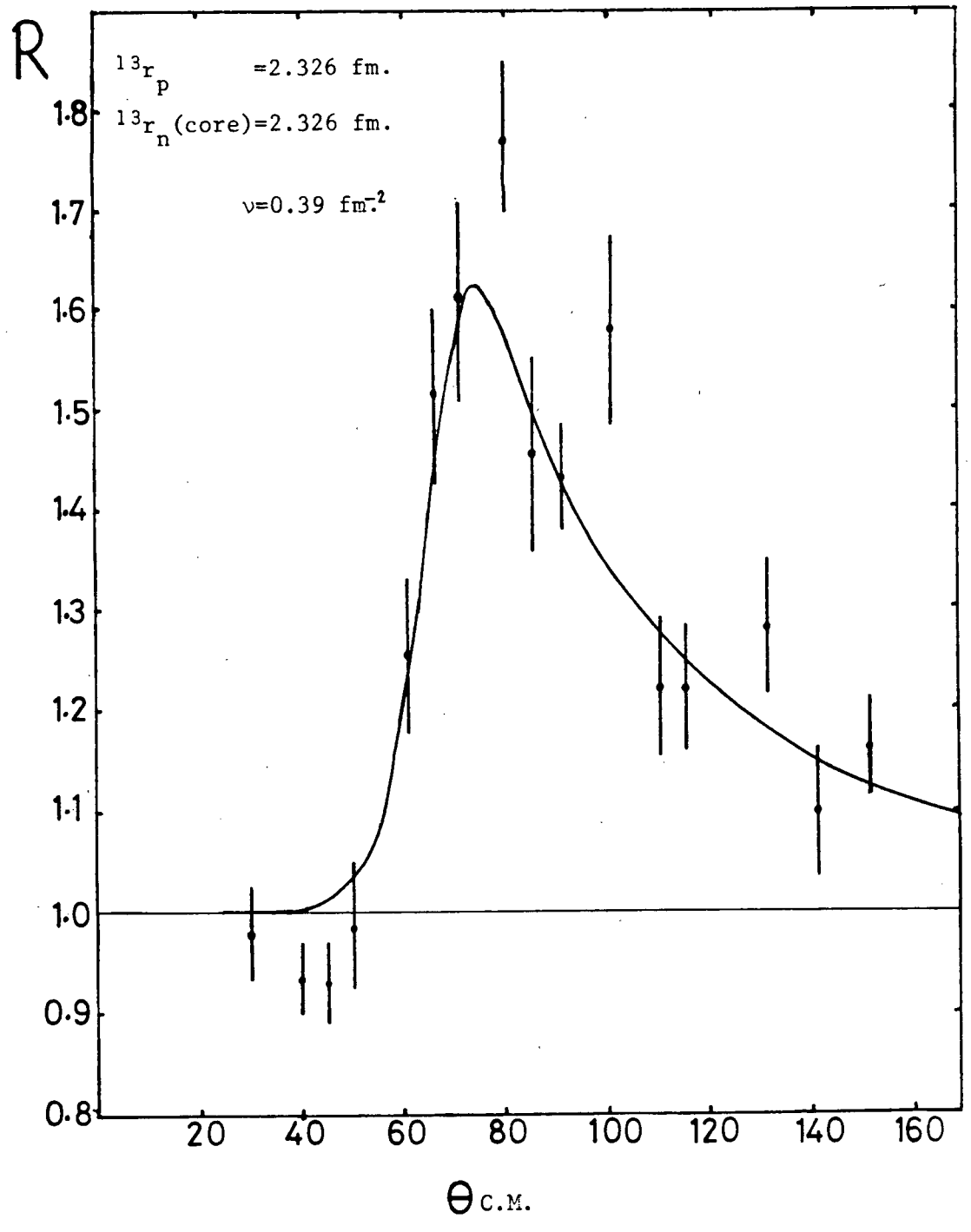

Figure 19. χ^2 Curves for
Valence Neutron + Core Model.

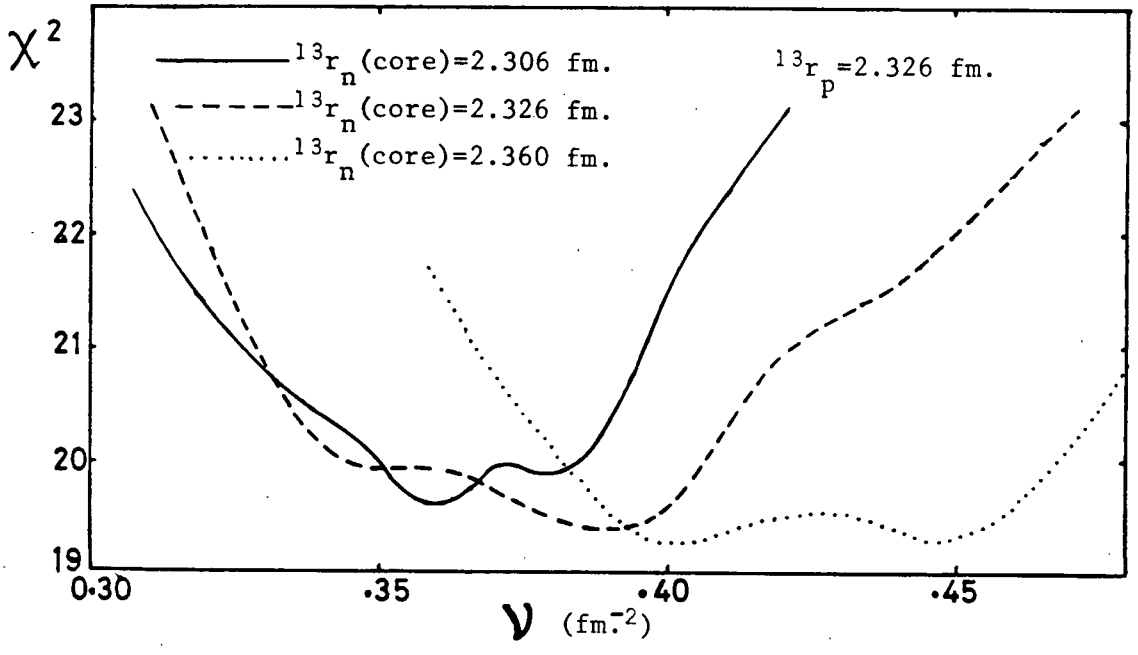

defined as midway between the two pionts where χ^2 is 1 greater than the lowest value. Evaluating the rms. radii, for the total neutron distributions gives $^{13}r_n$=2.354±.014, 2.365±.019 and 2.370±.020 fm. for r (core)=2.306, 2.326 and 2.360 fm. respectively. The best fit rms. radius remains almost constant. This suggests that the sensitivity is to the rms. radius of the neutron distribution and not to the detailed structure.

Calculations of R were therefore made with different neutron distributions of the same total rms. radius=2.36 fm. The distributions were formed by combining p-wave neutron wavefunctions of different well strength with modified Gaussian distributions of differing rms. radii. The proton distribution of ^{13}C measured by Heisenberg is represented as a modified Gaussian distribution, but α differs by about 6% from the shell model value. The variations in the distribution for $^{13}r_n$ (Fig. 20) used here are approximately equivalent to varying α by ±10%. The resulting distributions for R are very similar and the total χ^2 varies by less than 1.5 (Table VII). This suggests that it is possible to obtain a measurement of $^{13}r_n$ which is not significantly dependent on uncertainties in the form of the neutron distribution. Combination with information from higher energy pion scattering and with pionic atom data may permit measurement of more detailed structure in the distribution.

b) Neutron Distribution rms. Radius

Calculations of R were made, using a modified Gaussian distribution for both the neutrons and protons, varying both $^{13}r_p$ and $^{13}r_n$. A χ^2 contour plot (Fig 21) was produced from the

Figure 20. ^{13}C Neutron Distributions with Equal rms. Radius

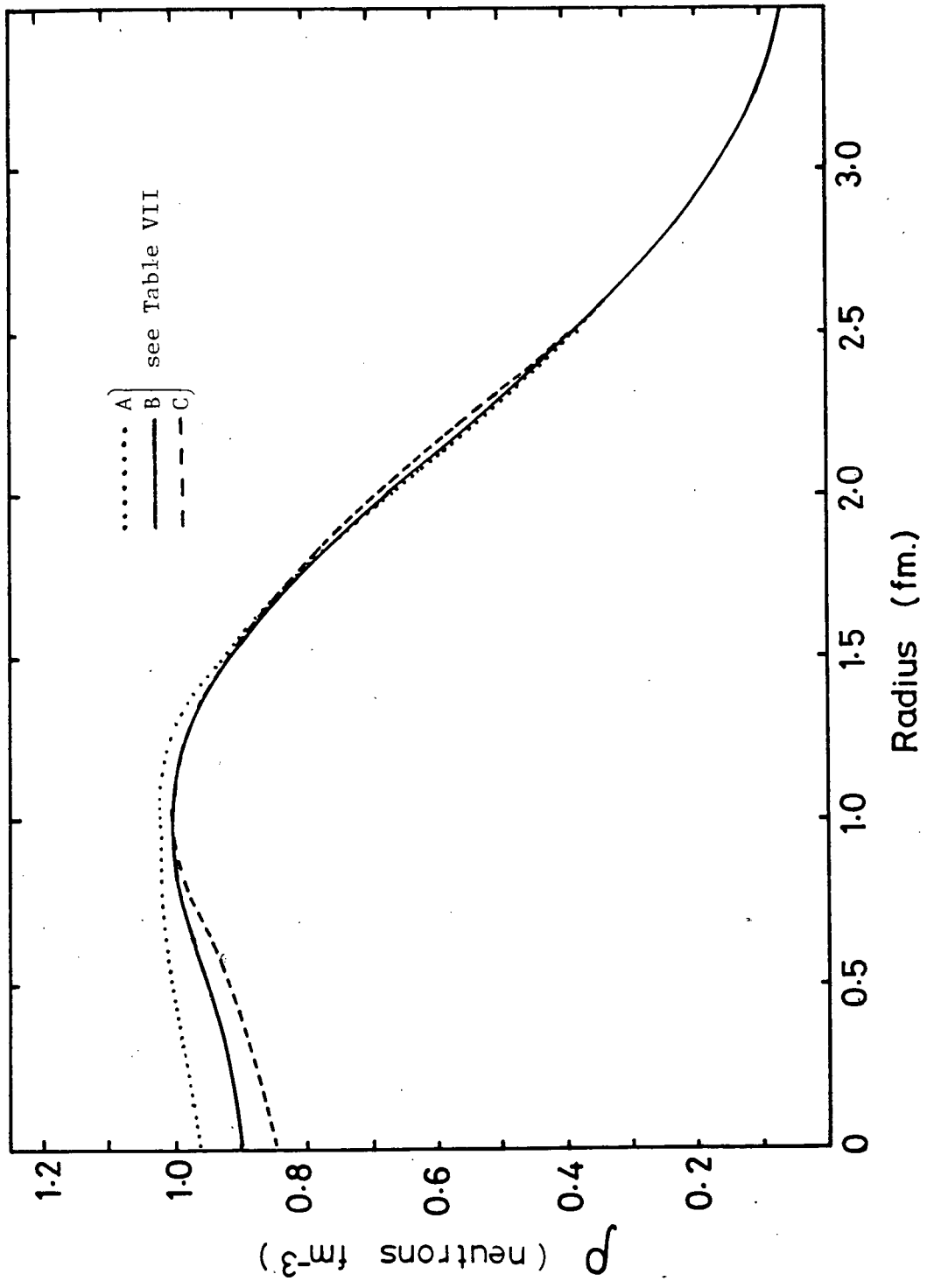

Table VII. Results of Calculations Using Different Neutron Distributions with Equal rms. Radius.

Line Fig 20	r_n (core) (fm.)	ν (fm.$^{-2}$)	χ^2
A	2.280	.32	20.77
	2.306	.353	19.81
	2.340	.41	19.40
B	Gaussian distribution		19.30
C	2.380	.50	19.93

Figure 21. χ^2 Contour Plot from Optical Potential Calculations using Parameter Set A.

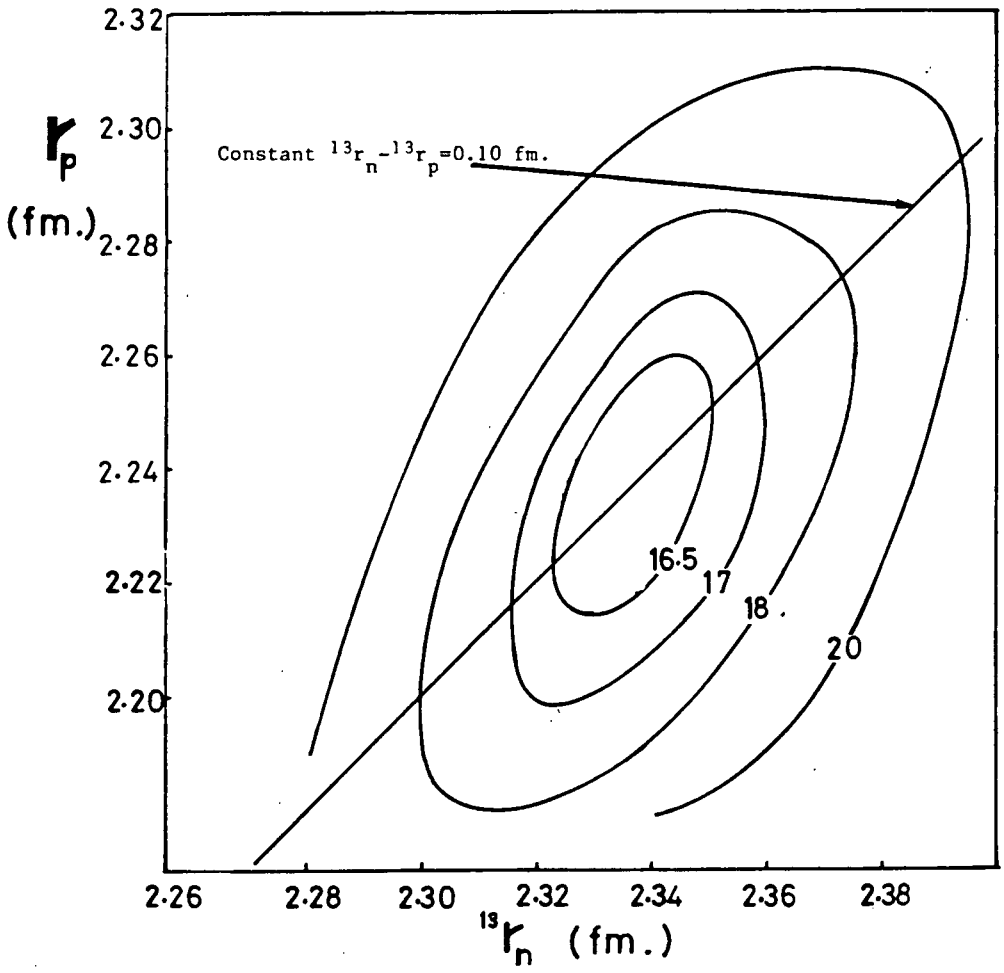

results (Figs 22 and 23). The value of $^{13}r_n$ at the χ^2 minimum changes from 2.370±.022 fm. at $^{13}r_p$ = 2.306 fm. to 2.337±.025 fm. at $^{13}r_p$ = 2.240 fm. The quantity $^{13}r_n - ^{13}r_p$ correspondingly changes from .064 fm. to .103 fm. The measurement of $^{13}r_n$ is therefore slightly dependent on the value of $^{13}r_p$ assumed. The χ^2 contour shows, however, that the π^- is more sensitive to the neutron distribution than the proton distribution.

Some tests were made of the dependence of the measurement of $^{13}r_n$ on the optical potential parameters. The proton radius was fixed at 2.306 fm. Two additional parameter sets were used (B and C, Table VI). Set B is SMC Set 1 (no variation of B_o and C_o). Set C is SMC Set 1 with the Ericson-Ericson parameter, λ, changed to 0.6. The fits to the ^{12}C cross section are shown in Fig. 17. The resulting χ^2 (Fig. 24) give $^{13}r_n$=2.374±.015 fm. and 2.387±.016 fm. for sets B and C respectively.

The dependence on the value of $^{12}r_c$ used was investigated by performing the calculations with $^{12}r_n = ^{12}r_p$=2.300 fm. Parameter set A was used with $^{13}r_p$=2.280 fm. The resulting χ^2 minimum (Fig. 24, curve D) is at $^{13}r_n$=2.344 fm. The two cases, $^{12}r_p$=2.326 fm. and $^{12}r_p$=2.305 fm. therefore both give values of $^{13}r_n - ^{12}r_p$ = .44 fm. . This demonstrates the measurement of $^{13}r_n$ is relative to the size ^{12}C assumed.

Figure 22. Results of Optical Potential Calculations with $^{13}r_p = 2.306$ fm.

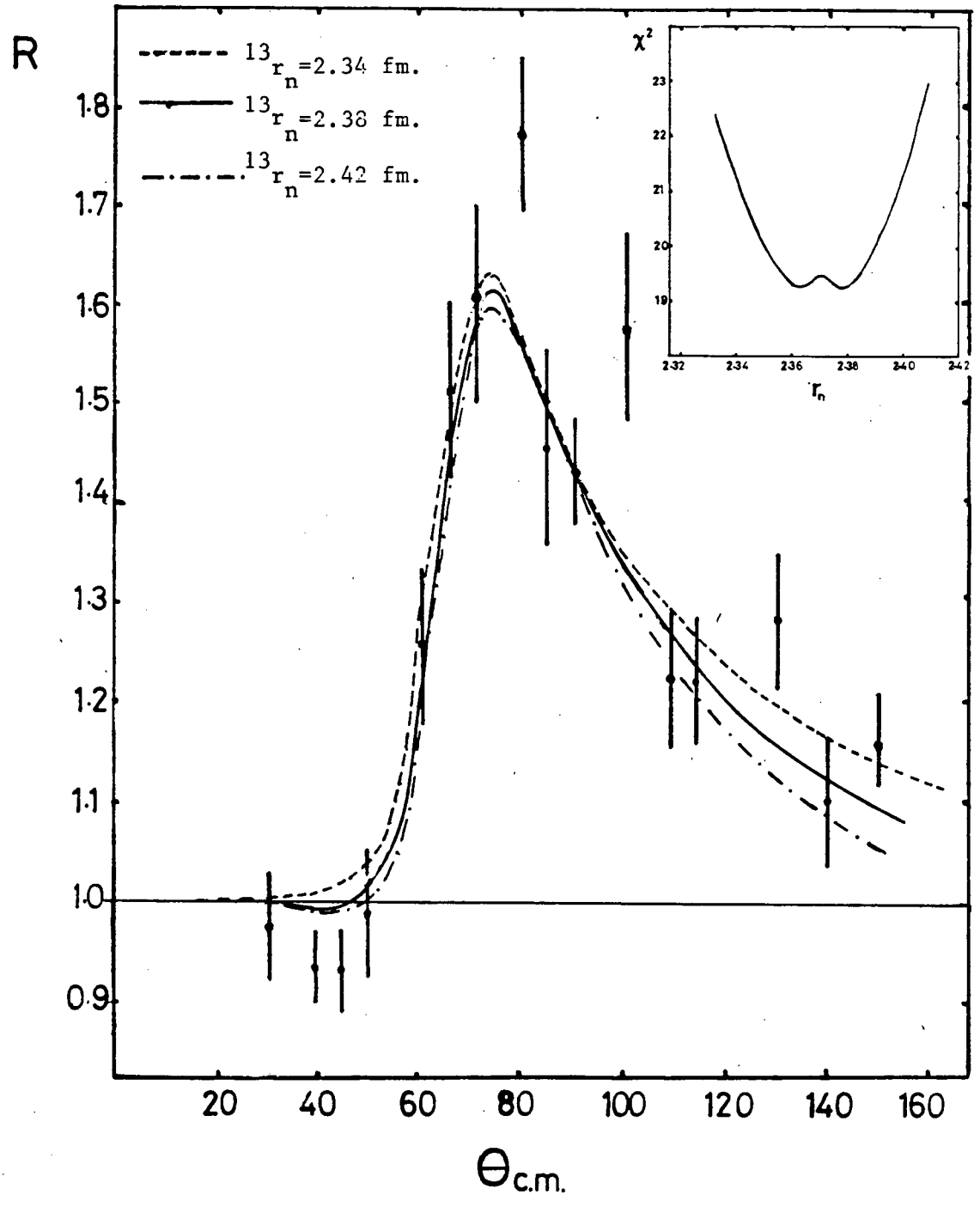

Figure 23. Results of Optical Potential Calculations with $^{13}r_p = 2.240$ fm.

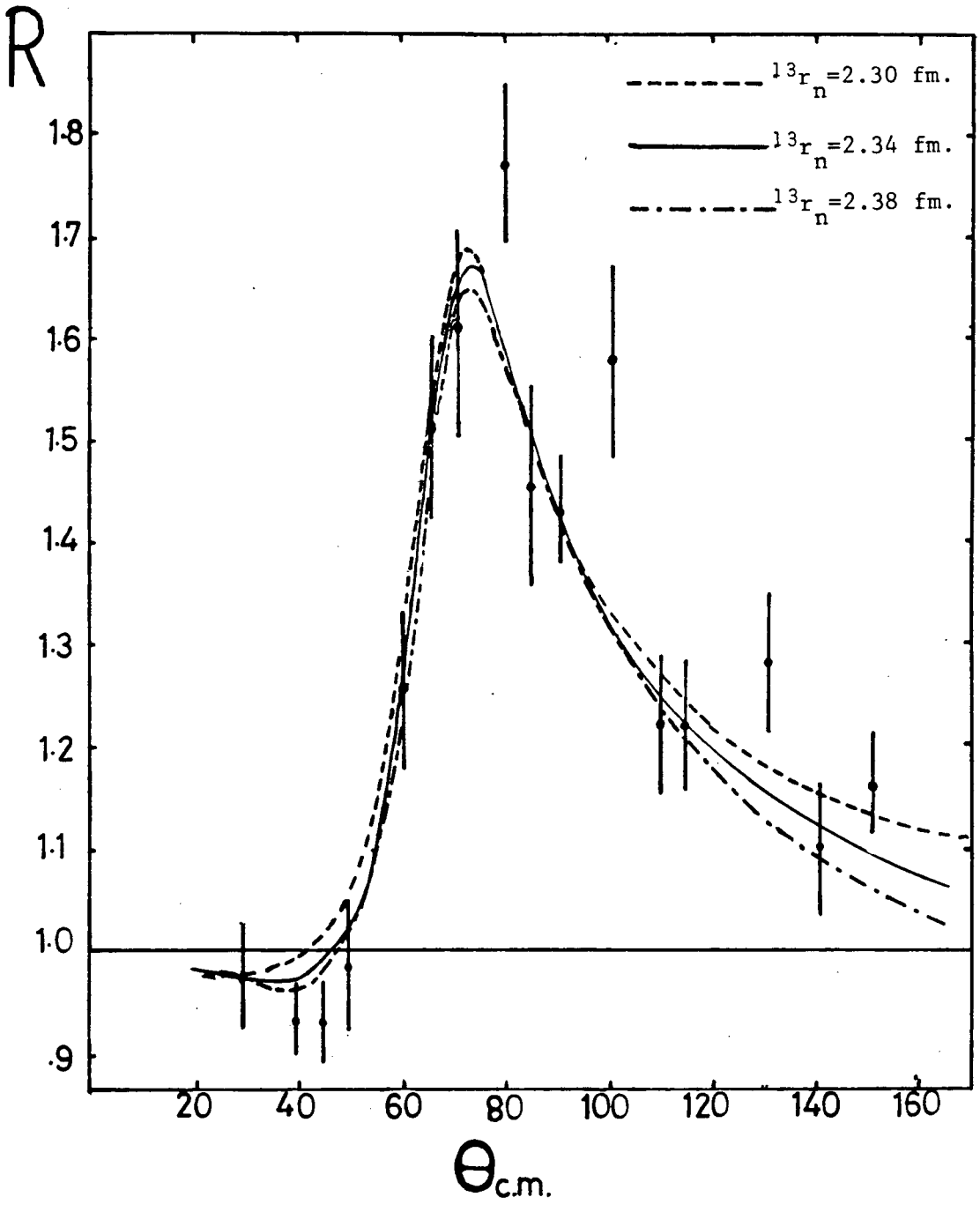

Figure 24. χ^2 curves of Optical Potential Calculations with Parameter Sets A, B and C.

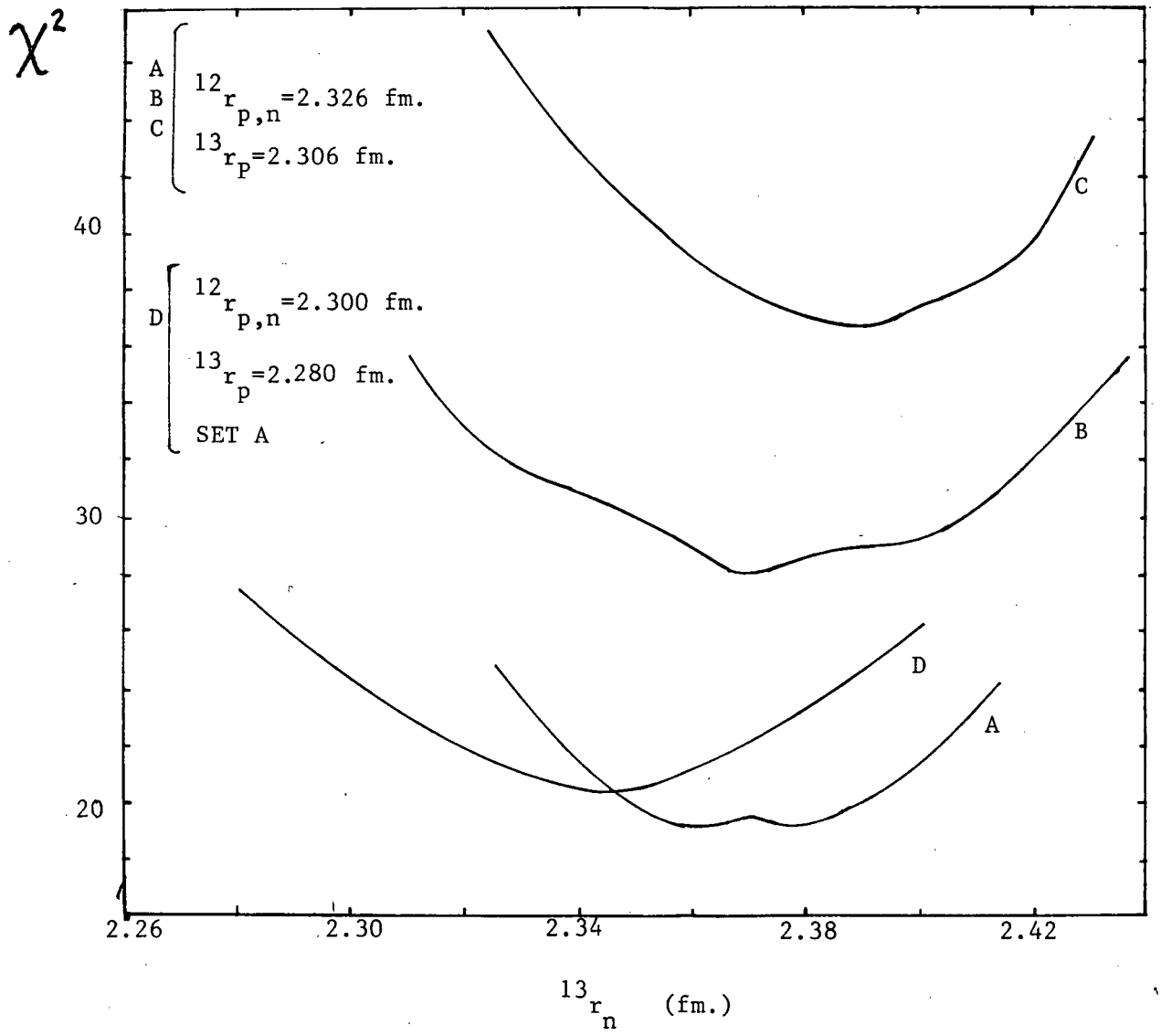

CHAPTER V

Summary and Discussion

The elastic scattering differential cross section ratios of 29 MeV π^- on $^{13}C/^{12}C$ were measured at angles from 30° to 150°. Since the measurement was a relative one the errors on the ratio are purely statistical. A large peak in the ratio at about 80° shows that the π^- is more sensitive to the effects of the valence neutron than π^+ at 50 MeV, where the distribution is quite flat.

The peak in the distribution is due to a change in the structure of the s-p interference minimum between ^{12}C and ^{13}C, which is due mainly to the large s-wave π^-n interaction. In Chapter IV, section 1, the π-nucleus interaction was represented by a sum of πN scattering amplitudes. It was shown that the data are fit quite well with this simple model if one parameter, the relative amount of s and p wave scattering, is allowed to vary. This suggests that in using a detailed optical potential calculation any errors or uncertainties in the potential will cancel to a large extent since they will produce the same effect in both nuclei. In this way, nuclear structure information such as density distributions may be isolated in the interpretation if the calculation produces the correct behaviour for variations in the nuclear structure.

A 6 neutron + harmonic oscillator valence neutron model was used for the neutron distribution of ^{13}C. It was found that the optical potential calculations were insensitive to the size of the core but depended largely on the neutron rms. radius. A

measurement of the ^{13}C neutron rms. radius was made and some tests were made for dependence on the optical potential parameters. For the three sets of parameters used, values of ^{13}C rms. radius of 2.370±.022, 2.374±.015 and 2.387±.016 fm. were found. Errors due to the uncertainty in $^{13}r_p - ^{12}r_p$, as measured by Heisenberg are negligible. The values of $^{13}r_n$ found using different optical potential parameters and different neutron distributions span from 2.354 fm. to 2.387 fm. The value 2.387 has a much larger χ^2 than the others. Leaving out this measurement the neutron rms. radius is measured to be 2.365±.025 fm. where the errors quoted are the range covered by standard deviations of the remaining measurements including those with the neutron + core model.

The reliability of this method of measuring neutron radii should be tested. The proton radius differences between neighbouring isotones may be measured where accurate values already exist from electron scattering. In this case π^+ would be used and the situation is then analogous to the present experiment apart from Coulomb effects. Secondly a measurement of the neutron radius should be made on an isotope such as Ca^{48} where previous measurements and Hartree Foch calculations exist.

By combining with information from higher energy pion scattering and pionic atom data , where the surface density only is sampled , it may be possible to obtain more detailed information on the neutron density distribution.

BIBLIOGRAPHY

1.) M. Ericson and T.E.O. Ericson,
Ann. Phys. 36, 323 (1966)

2.) J. Eisenberg, J. Hufner and E.J. Moniz,
Phys. Lett. 47B, 381 (1973)

3.) M. Krell and T.E.O. Ericson, Nucl. Phys. B11, 521 (1969)

4.) J. Hüfner, Physics Reports 21C, 1 (1975)

5.) K. Stricker, H. McManus and J. Carr,
Phys. Rev. C19, 929 (1979),

6.) W. Gibbs, B.F. Gibson and G.J. Stephenson,
Phys. Rev. Lett. 39, 1317 (1977)

7.) N.J. Digiacomo, Phys. Lett. 66B, 421 (1977)

8.) G.K. Varma and L. Zamick, Nucl. Phys. A306, 343 (1978)

9.) G.K. Varma, Bull. Am. Phys. Soc. 22, 1009 (1977)

10.) G.K. Varma and L. Zamick, Phys. Rev. C16, 308 (1977)

11.) J.C. Lombardi et al., Nucl. Phys. A188, 103 (1972)
G.W. Greenless et al., Phys. Rev. 20, 1063 (1970);
Phys. Rev. C3, 1560 (1971)

12.) G.M. Lerner et al., Phys. Rev. C12, 778 (1975)

13.) B. Tatischeff et al., Phys. Rev. C5, 234 (1972)

I. Brissaud et al., Nucl. Phys. A191, 145,

14.) G.D. Alkazov et al., Nucl. Phys. A280, 365 (1977)

15.) M.J. Jackobson et al., Phys. Rev. Lett. 38, 1201 (1977)

16.) J.W. Negele, Phys. Rev. C1, 1260 (1970)

17.) A. Abashian, R. Cool and J.W. Cronin,
Phys. Rev. 104, 855 (1956)

18.) B.W. Allerdice et al., Nucl. Phys. A209, 1 (1973)

19.) M.D. Cooper, A.I.P. Conf. Proc. 33, 237 (1976)

20.) J. Jansen et al., Phys. Lett. 77B, 359 (1978)

21.) M.M. Sternheim and Kwang-Bock Yoo,
Phys. Rev. Lett. 41,1781,(1978)

22.) S.A. Dytman et al., Phys. Rev. C18, 2316 (1978)

23.) G. Rowe, M. Salomon and R.H. Landau,
Phys. Rev. 18C, 584 (1978)

24.) K. Shortt, private communication.

25.) T. Marks, private communication.

26.) J.F. Janni, Air Force Weapons Laboratory,
Technical Report N° AWFL-TR-65-150

27.) E. Rost, private communication.

28.) R.R. Johnson et al., to be published.

29.) M. Thiess, Phys. Lett. 63B, 43 (1976)

30.) I. Sick and J.S. McCarthy, Nucl. Phys. A150,631 (1970)

31.) H. Cranell et al., Nucl. Phys. A103, 677 (1967)

32.) C.S. Yang et al., Nucl. Phys. A162, 71 (1971)

33.) J. Heisenberg, J.S. McCarthy and I. Sick,
Nucl. Phys. A157, 435 (1979)